

Time lapse seismic analysis of the Tohoku-Oki 2011 earthquake

M.Landrø¹, S.Kodaira², T.Fujiwara², T.No², W.Weibull³ and B.Arntsen⁴

¹NTNU, Department of Electronic Systems, Trondheim, Norway

²R&D Center for Earthquake and Tsunami, Japan Agency for Marine-Earth Science and Technology, Yokohama, Japan.

³University of Stavanger, Department of Petroleum Engineering and Applied Geophysics, Stavanger, Norway.

⁴NTNU, Department of Geoscience and Petroleum, Trondheim, Norway

Corresponding author: Martin Landrø (martin.landro@ntnu.no)

Key Points:

- Time lapse seismic analysis shows seabed subsidence and uplift
- Estimate a stretching of sedimentary rocks of up to 6 m at the shelf
- Indication of new faults or reactivation of faults within sediments
- Seismic velocity decreases at the shelf and increases closer to the trench axis

19 Abstract

20 A detailed time lapse seismic analysis of subsurface movements is presented using seismic 2D
21 lines acquired prior to and after the Tohoku-Oki earthquake offshore Japan in 2011. Estimated
22 movements of the seabed from the time lapse seismic data corresponds well with estimations using
23 bathymetric data. On the shelf, we find seabed subsidence of up to 8-9 m, and closer to the Japan
24 trench, we find a seabed uplift of more than 10 m. Along the 100 km long 2D seismic line, we find
25 alternating subsidence and uplift. We find horizontal displacements at the seabed that are
26 significantly larger, up to 40-50 m, however these estimates are more uncertain. Close to the Japan
27 trench, these horizontal displacements are practically opposite in direction (pointing towards the
28 trench from both sides) and large (~15 m). At the sediment-basement interface, we estimate
29 vertical subsidence of two independent large blocks (each 4 km wide) to be up to 14 m. This means
30 that the sediment package in this region has been stretched by 5-6 m. This type of overburden
31 stretching is similar to hydrocarbon reservoirs that compact due to production and produce
32 corresponding overburden stretching. Several examples of new faults, new layering and orientation
33 of sedimentary layers are found. Implications for subsurface storage of CO₂ in areas close to
34 subduction zones are also discussed.

35

36 1 Introduction

37 Co-seismic fault slip behaviour of the 2011 Tohoku-Oki earthquake has been intensively studied
38 by seismological, geophysical, geological, geodetic and tsunami wave data. Although various
39 models of co-seismic slip distributions (*e.g.*, *Fujii et al., 2011; Lay et al., 2011; Ide et al., 2011;*
40 *Satake et al., 2013*) have been suggested, there is a general consensus that a large co-seismic
41 fault slip of more than 50 m reached the trench axis of the central part of the Japan Trench. This
42 large co-seismic slip generates a large seafloor displacement (*Sato et al., 2011; Kido et al., 2011;*
43 *Ito et al., 2011*) which is considered to be the major cause of the large tsunami wave hitting the
44 coastline of the eastern part of Japan. In addition to those studies, data from several marine
45 geological and geophysical studies demonstrate more direct evidences showing trench breaching
46 co-seismic slip (*Fujiwara et al., 2011 and Kodaira et al., 2012*).

47

48 Differential bathymetry measured before and after the 2011 Tohoku-Oki earthquake clearly
49 shows that the sea floor on the outermost part of the landward of slope to the trench moved ~50
50 m east-southeast towards the trench and ~7 to 10 m upward (*Fujiwara et al., 2011*). The seafloor
51 displacements terminate at the trench axis. Co-seismic structural changes of the sedimentary
52 section above the plate interface at the trench axis are observed by visual comparison of seismic
53 sections acquired along the same profile (*Kodaira et al., 2012*). The differential bathymetry and
54 seismic data are the first direct evidences showing co-seismic fault rupture of a subduction zone
55 where an earthquake breaches the seafloor at the trench axis. However, quantitative analysis of
56 co-seismic structural changes near the trench in order to examine co-seismic deformation
57 processes has not been performed so far, due to challenges related to time lapse analysis of the
58 seismic data. Some of these challenges include variations in acquisition set up and positioning
59 issues causing lower repeatability compared to conventional time lapse seismic surveys.

60 The main objective of this paper is to investigate if a detailed, quantitative time lapse seismic
61 analysis of two datasets acquired before and after the earthquake, can reveal new insight into
62 rock movements and changes in rock properties. For this purpose we reprocessed the two

63 datasets, estimated seismic velocities independently for the two surveys, and obtained two
64 similar data sets better suited for time lapse seismic analysis. With our background from 4D
65 seismic analysis (*Landrø et al., 1999; Landrø, 2001, Landrø, 2015*) and seismic imaging
66 (*Weibull and Arntsen, 2013*), we want to explore how this knowledge can be used for improved
67 understanding and mapping of earthquakes.

68
69 **In the 2005 IPCC special report on carbon capture and storage (IPCC, 2005) there is a separate**
70 **chapter on the geographical relationship between the sources of CO₂-emissions and storage**
71 **opportunities. Areas considered as highly prospective are sedimentary basins far away from**
72 **subduction zones. However, some of the next category of potential storage sites, characterized as**
73 **prospective sedimentary basins are close major subduction zones, as for instance offshore Japan**
74 **and Indonesia. Apart from one minor demonstration project (Tanaka et al., 2017) there are no**
75 **CO₂-storage projects close to our study area. Our motivation for linking our time-lapse analysis**
76 **of the Tohoku 2011 earthquake is therefore futuristic: Since the CO₂-sources in Japan are**
77 **significant, there might be a need to store significant amount of CO₂ offshore Japan. In addition**
78 **to this, a time-lapse seismic analysis of one of the largest recent earthquake, is of general interest**
79 **for other potential storage sites on earth.**

80
81 **In our analysis we will assume that most of the movements between the seismic surveys acquired**
82 **in 1999 and 2011 is caused by the huge Tohoku-Oki earthquake in 2011. Other earthquakes that**
83 **occurred within the timeframe between the monitor and base surveys are significantly weaker,**
84 **but since the time interval between the two surveys is more than 10 years, we cannot disregard**
85 **that some of the movements we have identified are not caused by the major 2011-event.**

86 **2 Tectonic setting**

87 The Japan Trench is a convergent plate boundary where the Pacific plate subducts beneath the
88 volcanic arc of the northern Japan, and extends from the junction with the Kuril Trench at the
89 north to the junction with the Izu-Bonin Trench at the south. The geological structures of the
90 Japan Trench subduction zone have been well-studied by seismic surveys and ocean drilling
91 since the last three decades. Based on the data from the seismic and the ocean drilling, previous
92 geological and seismic studies commonly divided the forearc region of the Japan Trench into
93 four areas, which consists of the deep sea terrace, the upper slope, middle slope and lower slope
94 from landward to the trench axis (e.g., von Huene and Culotta, 1989; von Huene and Lallemand,
95 1990). The deep sea terrace is a gently deepened slope at water depth down to ~ 3 km, and
96 continues to a rather steep upper slope extending from water depths of about 3 km to 5 km. The
97 middle slope generally shows a terrace-like, locally narrow, gentle slope with water depth around
98 ~ 5km. At the trench-ward of the middle slope, the steep and rugged lower slope continues to the
99 trench axis. The trench axis shows intermittent narrow and flat basin, which locally consists of
100 graben-fill sediments. The oceanic crust entering the trench is characterized as clear horst-and-
101 graben structure due to bending the subducted oceanic plate. The horst-and-graben structure
102 seems to be growing even after the oceanic crust is subducted (Tsuru et al., 2002; Kodaira et al.,
103 2017).

104 The results of ocean drilling combined with seismic images show Plio-Pleistocene and Miocene
105 sediments that unconformably overlie the Cretaceous continental block at the shallow part of the
106 deep sea terrace and the upper slope (Tamaki et al., 1990; Jolivet and Tamaki, 1992). The
107 shallow part of the Plio-Pleistocene strata from the deep sea terrace to the upper slope are

108 deformed by normal faults, which locally extend to the sea floor. Previous studies proposed that
 109 the normal fault system have formed due to tectonic erosion of the base of the overriding plate
 110 by subduction of a rough basement geometry of the oceanic crust, which cause a continental
 111 subsidence in the fore arc (von Huene and Lallemand, 1990; von Huene et al, 1994). However,
 112 the tectonic process to form the extension (normal faulted) structure in the fore arc region of the
 113 convergent plate boundary is still debated.

114 A prism-shaped low-velocity wedge at the trench-ward end of the overriding block has been
 115 reported as a characteristic structure of the Japan Trench since von Huene et al. (1994) have
 116 shown its fine seismic image. The prism-shaped low-velocity wedge is roughly 20 – 30 km wide
 117 and 3 – 4 km thick with seismic velocities ranging between 2–3 km/s. Compilations of
 118 distribution of the prism-shaped low-velocity wedge show that those low-velocity wedges mostly
 119 developed at the norther part of the Japan Trench (i.e., north of 37.5° N) (Tsuru et al., 2002;
 120 Kodaira et al., 2017). In the southern part of the Japan Trench, instead of the prism-shaped low-
 121 velocity wedge, a low-velocity (3 – 4 km/s) elongated sedimentary unit extends in the downdip
 122 direction along the plate boundary interface. Recent ocean drilling results show that the trench-
 123 ward tip of the prism-shaped low-velocity wedge mostly consists of pelagic sediments (Chester
 124 et al., 2013)

125
126

127 **3 Data acquisition of 1999 and 2011 seismic data sets**

128

129 The baseline 2D seismic (MY101) was acquired in 1999. Table 1 gives a summary of the
 130 acquisition parameters. A source array consisting of 6 identical subarrays each with a volume of
 131 1500 cubic inches was used. The gun depth was 10 m, and the streamer depth was 15 m. The
 132 streamer length was 3600 m, and a shot point interval of 50 m was used. The receiver interval
 133 was 25 m, and a total of 144 channels were recorded. The monitor survey (D13) was acquired in
 134 May 2011, after the Tohoku-Oki earthquake. A summary of acquisition parameters is given in
 135 Table 2. A source array consisting of 4 identical subarrays with a volume of 1950 cubic inches
 136 was used. This means that the total source volume of the monitor survey (7800 cu. in.) is
 137 somewhat less than that of the baseline survey (9000 cu. in.). Hence we expect a somewhat
 138 weaker signal for the monitor survey (10 % reduction). The gun depth was the same as for the
 139 1999 survey (10 m), but the streamer depth was increased from 15 to 21 m. The streamer length
 140 for the monitor survey in 2011 was 5500 m, the receiver interval was 12.5 m and the total
 141 number of channels was 444. The location of the 2D seismic line (denoted D13 and MY101) is
 142 shown in Figure 1. The difference in cable depths for the two surveys results in slightly different
 143 spectral compositions, due to the ghost effects. The source ghost spectrum is given by
 144 (*Amundsen and Landrø, 2010*)

$$145 \quad G_{source}(f) = \left| 2 \sin \left(\frac{2\pi f z}{c} \right) \right| \quad (1)$$

146 Where f denotes frequency, z is the source depth and c is the water velocity. The source ghost
 147 spectrum is shown in Figure 2, and is identical for the two surveys. The receiver ghost spectra
 148 will however be slightly different as shown in Figure 2. Since the receiver depth is increased
 149 from the first to the second survey, the first notch in the receiver ghost spectrum is shifted from
 150 50 to 37 Hz (assuming a water velocity of 1500 m/s). This difference means that there will be a

151 significant difference between the two datasets for frequencies between 30 and 60 Hz. To some
152 extent, it is possible to compensate for this by using Wiener-type match filters (as described in
153 the next section). However, especially close to the receiver ghost notches (36.6 and 50 Hz) it is
154 practically impossible to compensate for loss of data caused by the ghost notches.

155 **4 Time lapse processing of the data**

156 4.1 Preprocessing, regularization and key processing steps

157 Interpolation was used to make the 1999 and 2011 datasets conform to a common regular
158 geometry. A 2D deterministic deconvolution (time and angle dependent) was used to modify the
159 wavelet in the 2011 dataset, which contained significant bubble reverberations. The target
160 wavelet used was a Ricker wavelet with a dominant frequency of 20 Hz. Following this
161 procedure, one global match filter was derived to match the 1999 dataset to the 2011 dataset.
162 Totally 22800 traces were used to compute an average Wiener filter. This filter was then applied
163 to the 1999 dataset, in order to make it as similar as possible to the 2011 dataset. The data were
164 then binned using a CMP (Common MidPoint) interval of 12.5 m, leading to 7740 CMP
165 positions, with a fold of 36 traces within each CMP. The offset interval for the CMP gathers was
166 100 m. Velocities were picked independently for the two datasets using an auto-picker
167 algorithm. The auto-picked velocities were reliable only down to the top basement reflection
168 (Figure 3). Where the signal to noise ratio was poor and where there were strong free surface
169 multiples, the auto picked velocities were substituted by a constant stacking velocity of 2200
170 m/s. The picked velocities were smoothed laterally using a 500 m running average window.

171 The resultant two sets of stacking velocities were smoothed and used for prestack time
172 migration of the respective seismic datasets. The reason for using two sets of stacking velocities
173 for migrating the data is that the velocities found were significantly different between 1999 and
174 2011. Using only one velocity or an average velocity leads to a pronounced under or
175 overcorrection of the prestack seismic gathers. This could in turn lead to large differences
176 between the seismic images between 1999 and 2011, and mask the true time lapse effects.
177 Another advantage of using two different velocity fields, is that the velocity differences contain
178 information that can be used as an independent source of information in the analysis. The stacked
179 version of the baseline survey from 1999 is shown in Figure 3. The seabed reflection is clearly
180 mapped, as well as the basement. The Japan trench is at the maximum water depth around 72 km
181 in distance (measured from the start of the line).

182 4.2 Basic assumptions and precautions

183 Velocity variations in the water column are a major uncertainty in the time lapse seismic
184 analysis. We tested both a 1% velocity increase and decrease in velocity between the two surveys
185 (Figure 5, bottom), and both tests lead to slightly more unrealistic estimates of the seabed uplift.
186 Therefore, we assumed no changes in water velocity between the two surveys. This is in good
187 agreement with the bathymetry data as shown in Figure 5 (top); i.e., a general trend of variation
188 of seafloor displacements estimated from the bathymetry and the seismic data shows a similar
189 pattern.

190
191 For some parts of the seismic line (especially between 14 and 18 km) there are significant errors
192 in source positions, up to 500 m. These positioning issues and how they impact the 4D seismic
193 analysis are further discussed in Appendix B.

194

195 **5 Geomechanical modeling and estimation of the dilation factor**

196 The importance of geomechanics related to time lapse seismic studies was realized when the first
 197 4D seismic results from the hydrocarbon chalk fields (Ekofisk and Valhall) in the southern North
 198 Sea came (Guilbot and Smith, 2002; Barkved and Kristiansen, 2005). Highly porous chalk is a
 199 weak reservoir rock and compaction larger than 10 m has been observed for the Ekofisk field,
 200 and a somewhat less seabed subsidence of up to 8 m (Guilbot and Smith, 2002). The fact that the
 201 reservoir compaction is larger than the seabed subsidence means that the rocks above the
 202 reservoir are stretched. The reservoir compaction is mainly caused by two effects in this case:
 203 First, the pore pressure decrease leads to compaction and second a chemical reaction between
 204 injected water and the chalk weakens the rock (water weakening), and this leads to compaction.
 205 The challenge for time lapse seismic analysis is that for rocks that undergoes either stretching or
 206 compaction, there are two unknown parameters: the thickness change and the velocity change.
 207 Landrø and Stammeijer (2004) showed that the relative time lapse seismic timeshift (dT/T) is
 208 directly related to the relative velocity change (dv/v) and the relative thickness change (dz/z) as:

$$209 \frac{dT}{T} = -\frac{dv}{v} + \frac{dz}{z} \quad (2)$$

210 Hatchell et al. (2005) and Røste et al. (2005) give a simple relation between the measured
 211 relative seismic timeshift (dT/T) and the stretching (dz/z) of the rocks:

$$212 \frac{dT}{T} = (1 + R) \frac{dz}{z}, \quad (3)$$

213 where $R = -\frac{dv/v}{dz/z}$, dz represents the stretching of the rocks, z is the thickness of the overburden
 214 rocks, and R is an empirical constant often referred to as the dilation factor. v is the average P-
 215 wave velocity and dv is the change caused by stretching or compaction. Hatchell and Bourne
 216 (2005) find R -values ranging between 1 and 5 based on time lapse seismic data acquired in the
 217 North Sea. In a more recent study, Røste et al. (2015) find R -values up to 20 for overburden
 218 rocks at the Snorre field, North Sea. In this work we estimate timeshifts (right hand side of
 219 equation 2) directly from the time lapse seismic data, and then a simple geomechanical modeling
 220 based on Geertsmaa's equation (Geertsmaa, 1973) is used to estimate dz/z . An alternative way to
 221 estimate R -factors directly from time lapse seismic data is to use AVO (Amplitude Versus
 222 Offset) techniques as described by Landrø and Stammeijer (2004).

225 **6 Results**

226 **6.1 Seabed displacement**

227 Figure 4 shows seismic sections covering the seabed reflection before and after the earthquake
 228 for the shelf (first 12 km of the line). The blue line represents the automatic picking of the
 229 maximum amplitude of the seabed reflection for the 1999-data, and the red line represents the
 230 same event for the 2011 data. An average time shift of approximately 10 ms is observed. Using

231 the same automatic picking method for the whole line we observe not only vertical shifts, but
232 also horizontal shifts.

233 Figure 5 (top) shows a comparison of estimated vertical seabed uplift from bathymetric data
234 (blue solid line) and time lapse seismic data (black solid line). We notice a good correlation
235 between the two techniques. A 625 m long lateral smoother has been applied to both data sets.
236 The time lapse seismic estimates are based on automatic picking of the maximum peak at the
237 seabed for the base and monitor seismic data-sets, followed by a direct subtraction. Conversion
238 into seabed uplift is done by assuming a constant water velocity of 1500 m/s. The brown solid
239 line shows the seabed position along the seismic line. **It is inherently challenging to estimate
240 error bars or uncertainties for the estimated seabed uplift. This is due to the fact that there are
241 several systematic error sources. One obvious error source is that the water velocity may change
242 between the base and monitor survey. This is discussed in detail in Appendix A. Based on this
243 we have picked a value of +/- 1 % to estimate the uncertainty related to varying water velocity.
244 This uncertainty is shown as a grey shaded area in Figure 5 (bottom). Uncertainties related to
245 positioning errors and a non-smooth sea bottom is discussed in Appendix B. We performed a
246 simple 3D seismic modeling exercise for a limited part of the line (the first 26 km) and used the
247 positioning errors and the seabed topography in this area to estimate traveltime errors (Figure
248 B3). These traveltime errors were then converted to systematic errors in the seabed uplift
249 estimations and are shown by the red shaded area in Figure 5 (bottom). We notice that these
250 positioning errors are less than the velocity induced errors apart for x-positions between 15 and
251 18 km.**

252
253 Based on these tests and comparison to the bathymetric data shown in Figure 5 (top), we
254 concluded that the most probable situation is that the water velocity has not changed significantly
255 between 1999 and 2011. To justify this choice further, we analyzed temperature and salinity
256 profiles from the same area acquired in 1999 and 2011. The analysis (Appendix A) shows that
257 the expected traveltime shifts caused by seasonal changes in water velocity are less than 3-4 ms,
258 and therefore less than the maximum estimated time shifts which are up to 10-12 ms at the
259 seabed and 50 ms at the top basement interface.

260 *Jiang and Simons (2016)* use a Bayesian framework to estimate seafloor uplift based on observed
261 tsunami waveforms close to the Japan coast. **If we compare our estimates of seabed uplift with
262 those (shown by red circles in Figure 5 (top)) presented by *Jiang and Simons (2016)* we observe
263 that our results have higher spatial resolution.** The result of Jiang and Simons is much smoother
264 and contains less spatial variations compared to both the time lapse seismic estimates as well as
265 the bathymetric results. It should be noted that the results of Jiang and Simons have been
266 extracted directly from Figure 6 in their paper, and that we have not received any numerical data
267 directly from them. There is therefore an uncertainty associated with the red circles in our Figure
268 5 (top) due to limited accuracy of picking correct values from the color bar in their Figure 6.

269
270 Figure 6 shows an example where horizontal movements are observable. By plotting the
271 estimated seabed position for both seismic surveys, we see that the red line (representing the data
272 after the earthquake) is shifted towards East for the area West of the Japan trench (between 60
273 and 73 km). For the area East of the trench (between 78 and 85 km) horizontal movement in the
274 opposite direction is observed (towards West). A simple way to estimate horizontal and vertical
275 displacements simultaneously is sketched in the insert of Figure 6, where the horizontal
276 displacement is simply approximated as finding the nearest position on the monitor data set with

277 the same z-coordinate as the base data set. The vertical displacement is estimated in a similar
278 manner: finding the vertical displacement directly (this is the same as the vertical displacement
279 estimated in Figure 5). As shown in the example, this simple method will not give correct
280 displacement vectors. However, as a quick and first order estimate of 2D displacements it might
281 serve as a useful tool, as shown in Figure 7. In this figure we have multiplied the estimated
282 displacement vectors by 50 for visualization purposes. We notice vertical displacements at the
283 shelf, followed by horizontal movements towards West between 28-32 km, towards East
284 between 36-48 km and 55-75 km. At the opposite side of the Japan trench, we observe horizontal
285 displacements towards West (80-92 km).

286
287

288 6.2 Variations in the sedimentary unit

289 At the continental shelf we find that the sedimentary unit beneath the seabed is stretched. This
290 stretch is not constant, but is found to be discontinuous and corresponding to vertical movements
291 within specific fault zones. This is illustrated in Figure 8, where we observe two distinct areas
292 (4.3-8.3 km and 10.5-14.5 km) where the subsidence at top basement and corresponding vertical
293 stretch is found to be particularly pronounced. In areas where a strong subsidence is observed,
294 we typically find that the seabed subsidence is less than at the basement level. This effect is
295 illustrated in Figure 9 (bottom) where a stretching of the sedimentary package is estimated. Time
296 shifts of the order of 40-45 ms are observed in these regions. In this case we cannot simply
297 convert such time shifts directly into vertical displacements, since the stretching of the sediments
298 leads to an unknown velocity decrease. We are faced with the challenge that we have two
299 unknowns (velocity change and vertical stretch) and one measurement: time shift. A common way
300 to solve this ambiguity is to introduce an empirical factor (the R -factor or the dilation factor)
301 relating the two unknowns and use geomechanical modeling to estimate it (Section 5). Using
302 geomechanical modeling (Gertsmaa, 1973; Fjær et al., 2008) in our case, we can model
303 displacements as shown in Figure X, we find an average R -factor equal to 6.7, and if this factor
304 is used, we find that the seabed subsidence and the subsidence of the top basement are similar,
305 but different, as shown in Figure 9a. The difference is more clearly presented in Figure 9b where
306 the estimated stretching of the sedimentary unit is shown. We recognize the two fault zones
307 related to subsiding areas (4-8 and 10-14 km). It should be stressed that the existence of these
308 faults is based on interpretation of the time lapse seismic data. We do not know the direct cause
309 of these faults, one possible mechanism could be horizontal stretching. Assuming that the R -
310 factor is constant and equal to 6.7 for the overburden, we can estimate the overburden velocity
311 changes (using equation 3 and the definition of R). Figure 9c shows a comparison between the
312 velocity changes estimated from the timeshifts (black line) and the average stacking velocity
313 difference (red line) estimated from conventional velocity analysis of the two seismic data sets.
314 We observe that there is a reasonably good correspondence between the two ways of velocity
315 change estimation within the subsidence zones (marked by vertical dashed lines in Figure 9b). A
316 rough estimate of the average deviation is 15 m/s within subsidence zone 1 and 10 m/s for
317 subsidence zone 2. However, outside these subsidence zones there are significant differences
318 between the two estimation methods. It should be stressed that the uncertainty related to stacking
319 velocity changes are significant, probably of the order of 25-50 m/s. There are also significant
320 uncertainties related to the geomechanical modeling, for instance the assumption of a cylindrical
321 symmetry, as well as the estimate of the radius of the cylinder.

322
323 Figure 10 (bottom) shows the estimated difference in stacking velocities between the two seismic
324 surveys. As expected, we find a velocity decrease at the shelf area (0-20 km). However, for most
325 of the slope towards the Japan trench, we find a velocity increase (20-50 km). For the area close
326 to the trench (50-85 km) we observe a velocity decrease for the upper half of the sedimentary
327 unit, followed by a velocity increase. It should be stressed that these velocity estimation is based
328 on an automatic picking method, not influenced by interpretation or velocity picking by hand.
329 However, it should be noted that if the automatic method fails, the velocity is simply assumed to
330 be 2200 m/s. This has a minor effect on the final velocity field.

331
332 Close to the trench axis, where the sediment package is relatively thick, we observe alignment of
333 some of the layers in an upward-East direction, as shown in Figure 11. We notice that some of
334 the horizontal interfaces (marked 1 and 2) on the figure are less pronounced and hard to interpret
335 after the earthquake. Furthermore, some of the upward dipping (towards East) interfaces are
336 more pronounced and stretch further towards the seabed after the earthquake (marked by 3 and 4
337 on the figure). This alignment is illustrated by the green arrows on the lower figure. A detailed
338 investigation of event 4 is shown in Figure 12, demonstrating that the dip has increased
339 somewhat after the earthquake.

340
341 Approximately 10 km East of the trench axis, we find an area where the estimated R -factor (or
342 the dilation factor) is negative. To our knowledge, this has not been observed for compacting or
343 expanding hydrocarbon reservoirs, and hence we consider this as an anomaly. We find that the
344 seabed timeshift is negative, while the top basement timeshift is close to zero. We interpret this
345 as a combination of vertical compaction and horizontal stretching. It is likely to assume that the
346 seabed uplift is caused by a vertical force from below. However, to explain the increased
347 traveltimes through the sediment package, we need an overall velocity decrease. So a combined
348 effect of horizontal stretching and a somewhat less vertical stretching might explain the observed
349 timeshifts and overall velocity decrease in the sediments. The horizontal stretching causes a
350 decrease in P-wave velocity and the vertical compaction causes a negative vertical strain,
351 yielding a negative dilation factor. Geomechanical modeling yields an R -factor equal to
352 approximately -16. The sediment package is relatively thin in this area, only 0.5 km.

353
354 An important and surprising result from the analysis of movements within the sedimentary units
355 is the small-scale (less than a kilometer) variations. Based on the time lapse seismic data we
356 interpret vertical movements of several meters and larger horizontal movements. Due to a
357 complex fault pattern and organization of the sedimentary units, our analysis indicate huge local
358 variations and movements in opposite directions. We think these details are extremely hard to
359 model and hence, time lapse seismic analysis can be used to achieve more detailed knowledge
360 about earthquakes occurring close to subduction zones. Furthermore we see that time lapse
361 seismic data has the potential to reveal detailed movements at the sedimentary-basement
362 interface, and that these details are smeared out at the top of the sedimentary unit.

363

364 **7 Implications for subsurface storage of CO₂ near subduction zones**

365 Several authors have discussed the influence of earthquakes on subsurface storage of CO₂.
366 Zoback and Gorelick (2012) argues that even small to moderate earthquakes threaten the seal

367 integrity of a CO₂ storage site. Juanes et al. (2012) argued that there is no geologic evidence that
368 seismicity causes fault leakage that would render large-scale storage of CO₂. One argument
369 given by Juanes et al. is that there is still large quantities of natural gas that is still present in the
370 subsurface. Verdon (2014) finds that 99 % of earthquake events related to fluid injection close to
371 hydrocarbon fields occur within a radius of 20 km from the injection well. Verdon states that an
372 induced event triggered well below the CO₂ storage volume will impose less risk for leakage as
373 an event in the sealing caprocks. Furthermore, Verdon stresses the importance of mapping faults
374 close to and below the CO₂ storage reservoir.

375 There is one CO₂-storage demonstration project being conducted in Tomakomai, Japan,
376 approximately 500 km NorthWest of the seismic line investigated in this paper. Tanaka et al.
377 (2017) describes that this project will store approximately 100 ktonnes of CO₂ per year into a
378 sandstone layer at approximately 1 km depth. The injection well is drilled from the harbor area in
379 Tomakomai into an offshore area approximately 4 km away. This project is monitored using
380 onshore seismometers, seabed seismometers and conventional 4D seismic. Another upcoming
381 CCS-project is the Gundih pilot project in Indonesia, where the plan is to inject CO₂ into the
382 Ngrayong sandstone formation at approximately 1 km depth (Tsuji et al., 2014). The Gundih
383 field is located in North Java, approximately 360 km North of the Sunda trench, so this is also an
384 example of a CO₂ injection project not too far from a major subduction zone.

385 Røste et al. (2007) give one example of fault reactivation interpreted from time-lapse seismic
386 data above a producing oil reservoir offshore Norway. From Figure 8 it is evident that there are
387 significant time shifts that are observed between 4.3 to 8.3 km and between 10.5 and 14.5 km.
388 We estimate the vertical displacement between 4.3 and 8.3 km to be roughly 15 m at top
389 basement, and that the corresponding subsidence at the seabed is roughly 10 m, indicating a
390 stretch of the sedimentary rocks of approximately 5 m. Outside this zone, this stretch (see Figure
391 9c) is practically zero, suggesting fault reactivation close to 4.3 and 8.3 km, respectively. It
392 should be noted that these vertical movements are at the continental shelf, some 50-60 km away
393 from the trench axis. Vertical movements of the order of meters within a sediment column, does
394 not necessarily mean that a CO₂-storage volume situated 1-2 km below seabed will leak.
395 However, the abrupt lateral changes that is observed from Figure 8, is a strong indication that
396 close to vertical faults might be created or reactivated by deep earthquakes. Chu et al. (2011)
397 estimated that the Tohoku earthquake originated from a small thrust event at a depth of 21 km,
398 that a few seconds later, evolved into a slower extremely large slip event. Juanes et al. (2012)
399 argue that the rheological properties of shallow sedimentary formations usually allow them to
400 undergo substantial deformation without establishing leaking pathways or localized faults. From
401 this work, we cannot conclude that new faults have been activated within the sediments by the
402 Tohoku earthquake. However, both vertical and horizontal movements of the seabed as observed
403 from time lapse bathymetry and seismic (Figure 5) show relatively abrupt variations along the
404 profile. Close to the sediment-basement interface these lateral variations are more pronounced.
405 Figure 9 b shows the estimated stretching of the sediment column caused by the earthquake, and
406 within the two subsidence zones, this stretch is up to 5-7 m, which is significant.

407 Based on these observations it is very hard to judge whether large vertical and horizontal
408 movements might cause leakage from a CO₂ storage site close to an active subduction zone.
409 Detailed geomechanical modeling that is beyond the scope of this work might give a deeper
410 insight into if leakage is likely to occur given that a major earthquake like the Tohoku occur at a

411 given distance from a CO₂ storage site. As pointed out by Verdon, a detailed and comprehensive
412 mapping of the storage reservoir as well as the underlying geology including pressure
413 distributions and fault patterns is crucial in such cases.

414 **8 Discussion**

415 In the processing of the time lapse seismic data, separate velocity tables were calculated for the
416 two datasets. This was done using an automatic picking procedure, and it was necessary to
417 flatten the prestack seismic gathers. Due to the limited offset range (0-3.6 km), the velocity
418 analysis is more unstable and less reliable for deep horizons, and especially close to the Japan
419 trench, where the water depth is close to 7 km. This means that the offset/depth ratio is only 0.5
420 close to the trench compared to 1.8 at the shelf. Hence, we should bear in mind that the accuracy
421 of the velocity differences decreases as water depth increases. Figure 10 shows a comparison
422 between the estimated seabed uplift and the estimated velocity changes. For comparison, we
423 have used a slightly longer smoothing window for the seabed uplift curve compared to that
424 shown in Figure 5. We notice a good correlation between seabed uplift and velocity change for
425 the first 50 km. Beyond this point there is no clear correlation between the two estimates. This
426 might be caused by the increased inaccuracy of the velocity estimates with depth. Another cause
427 might be variation in horizontal stretching along the line.

428 There are several uncertainties and precautions that should be addressed related to this work:
429 First, the repeatability of these data is not as good as time lapse seismic data acquired for the
430 purpose of monitoring subtle changes in a hydrocarbon reservoir. For instance, the position of
431 both the air gun sources and the streamers is not very accurate, and therefore we expect less
432 repeatable data, and the quantitative results should be handled with care. On the other hand, the
433 estimated changes in both velocity and timeshifts are one order of magnitude higher than those
434 normally observed for conventional 4D seismic surveys. We have tested how robust our
435 estimates are with respect to for instance positioning errors and changes of for instance water
436 velocity between the two surveys, and our conclusion is that our results are robust to such
437 changes.

438
439 Another observation supporting the assumption of no or minor velocity changes in the water
440 layer is that we observe a *positive* timeshift between the seabed reflection and the top basement
441 interface at the shelf (first 20 km of the seismic line). As described in section 5, this corresponds
442 to a stretching of the sedimentary rocks in this region, and the estimated *R*-factor (that is well
443 known from reservoir monitoring studies of compacting hydrocarbon fields (*Røste et al., 2005*
444 *and Hatchell et al., 2005*) is found to be close to 6.7. This is in good agreement with previous
445 work for sedimentary rocks. A change in water velocity will alter this value, and especially a
446 slight increase in water velocity leading to no subsidence at the shelf, will be very unlikely, since
447 we observe a stretching of the sedimentary rocks in this area.

448 *Osdal and Landrø (2011)* discuss methods for estimating velocity and water column thickness
449 variations directly from time lapse seismic data. Seasonal variations in water velocity measured
450 at a field (offshore Norway) where the water depth is 380 m are of the order of 3-4 m/s in
451 average. The velocity variations are largest for the upper 50 m, and tend to decrease with water
452 depth. Water velocity variations are mainly caused by temperature and salinity variations
453 (*Mackenzie, 1981*). *Lee and Cox (1966)* uses measured temperature profiles offshore California
454 to show that the temperature variations decrease significantly with water depth typically from 0.5
455 °C at 85 m to 0.014 °C at 2500 m water depth. Hence, it is reasonable to assume that seasonal

456 velocity changes for the whole water column in our case is minor, and probably less than +/- 1.5
457 m/s. This is further discussed in Appendix A.

458
459 The usefulness of repeated long 2D seismic lines were tested at the Troll field offshore Norway
460 using 8 2D lines acquired in 1997 and repeated in 2002 (Eiken and Tøndel, 2005). Timeshifts up
461 to 0.6 ms were estimated for an interface below the gas reservoir (situated at approximately 1500
462 m below sea level) with an accuracy of 0.1 ms. There are other examples of time lapse analysis
463 of repeated 2D seismic data (Landrø, 2011; Zadeh and Landrø, 2011) demonstrating that
464 especially timeshift analysis is robust despite significant variations in shot and streamer
465 positions. Another example where 2D and 3D time lapse results are compared can be found in
466 Bergman et al. (2011). Unfortunately the 2D seismic line is not intersecting the time lapse
467 seismic anomaly caused by the CO₂-injection at Ketzin (Germany). However, this study
468 confirms that the 2D time lapse seismic results are in agreement with the 3D results.

469
470 We think it is a good idea to acquire a third survey in the same area, using the same acquisition
471 parameters as in 2011, in order to investigate potential changes in for instance stress or rock
472 movements between 2011 and present.

473
474 A major shortcoming of this study is the lack of 3D seismic data. Especially when it comes to
475 estimates of rock volumes, the uncertainty is large. Our plan is to process the two remaining lines
476 shown in black in Figure 1, and from these results try to at least get an indication of crossline
477 stability or non-stability with regard to the results obtained so far. Furthermore, we think that a
478 similar analysis for the other two lines might serve as an input to a 3D tsunami modeling, which
479 can be compared to observations of the tsunami wave from 2011.

480
481 We interpret that the earthquake has caused a significant stretching (up to 7 m) of the relatively
482 thick (2 km) sediment package on the Japan Shelf. This amount of stretching is varying abruptly
483 along the seismic section, indicating that new faults are formed or reactivated. This means that
484 the risk of establishing leaking pathways from a CO₂ storage site within the sediments is
485 increased. However, since most CO₂-storage projects within soft sediments use an injection
486 pressure which is gentle or low, the risk of a blow-out like event from such a site is negligible.
487 Hence a recommendation for CO₂-storage within such formations is that the injection pressures
488 should be kept as low as possible, similar to that used on Sleipner, offshore Norway (Arts et al.
489 2008, and Landrø and Zumberge, 2017). For the current Tomakomai CCS demonstration project
490 (Tanaka et al., 2017) this is the case: The injection pressure is slightly above the hydrostatic
491 pressure within the sandstone layer where CO₂ is injected. In addition there are another
492 sandstone layer above the mudstone cap rock layer in this case, which will further diminish the
493 risk for CO₂ leakage into the sea.

494
495
496
497

498

499 **8 Conclusions**

500 Time lapse seismic analysis of two 2D lines crossing the Japan trench approximately 120 km
 501 North-East of the Tohoku-Oki earthquake epicenter shows clear evidence of fault slipping,
 502 extending all the way from the epicenter to the trench axis. From the time lapse seismic data we
 503 estimate an upward movement of the seabed of approximately 10-15 m close to the trench axis.
 504 Our observations fit with bathymetry data from the same area. Closer to the shelf, approximately
 505 60-70 km West of the trench axis a seabed subsidence of approximately 7 m is found. In the
 506 same area (which is 20 km in length), a corresponding subsidence of the top basement interface
 507 (approximately 2 km below the seabed) is estimated to be around 13-14 m. This estimate is
 508 based on observed timeshifts at this interface combined with geomechanical modeling. Estimated
 509 dilation factors (relative velocity change divided by vertical stretch) in this area is around 7,
 510 which fits nicely with observations from compacting hydrocarbon reservoirs. This subsidence
 511 correlates well with an estimated decrease in P-wave velocity of approximately 40 m/s in the
 512 area. East of the trench axis, we find an area where the estimated dilation factor is negative. This
 513 is most likely due to a combination of vertical compaction and horizontal stretching. The
 514 horizontal stretching causes a decrease in P-wave velocity and the vertical compaction causes a
 515 negative vertical strain, yielding a negative dilation factor.

516

517 Along the 100 km seismic line, we identify alternating areas (approximately 10 km in length)
 518 undergoing horizontal stretching and compaction close to the seabed. The correlation between
 519 horizontal stretching and compaction and observed velocity changes is not as clear as for the
 520 subsidence zone at the shelf. The two seismic data sets used in this study are not dedicated time
 521 lapse data sets aiming for a high degree of repeatability between the two surveys. Despite this,
 522 the quantitative results obtained from this study indicate that dedicated time lapse seismic
 523 surveys in this and other seismically active areas will be highly useful.

524

525 **Appendix A: Seasonal changes in water velocity**

526

527 There are vertical profiles of temperature and salinity (XCTD-data) available from the area close
 528 to the 2D seismic line used for this study. We used these data and the UNESCO equation (*Chen*
 529 *and Millero (1977)*, *Fofonoff and Millard (1983)* and *Wong and Zhu (1995)*) to estimate the
 530 water velocity as a function of depth for various calendar times. Figure A1 shows the velocity
 531 difference versus depth between the period 1 May to 31 May 2011 and the period 15 August to
 532 15 September 1999. Before taking the difference between the two velocity profiles we averaged
 533 over several geographical locations in the area. Figure A1 shows the velocity difference between
 534 2011 and 1999 (blue curve) and the corresponding cumulative average velocity difference (red
 535 curve). We notice that the average velocity difference for the first kilometer is less than 1 m/s.
 536 As another example we averaged the velocity difference over all years between 1999 and 2011,
 537 as shown in Figure A2. Also here, the cumulative average velocity difference at 1 km is
 538 relatively small, and less than 4 m/s. If we convert this into traveltime shift we find that an
 539 average velocity change of 4 m/s corresponds to a time lapse time shift of $dt = \frac{2z}{v} \frac{dv}{v} = 3.6ms$.

540

541 This is less than the maximum estimated time shifts from the time lapse seismic analysis which
 are more than 10 ms for the seabed interface and more than 50 ms for the top basement interface.

542 We realize that this is not a proof that water velocity changes might be neglected, however, it is
543 an indication that this effect is probably not the main time lapse signal in our analysis.

544

545 **Appendix B: Time-lapse processing of the MY101 (1999) and D13 (2011) seismic surveys**

546

547 The two 2D marine seismic surveys from 2009 and 2011 were not originally designed to be used
548 for high-precision time-lapse purposes. The repeatability of the source-receiver positions are not
549 perfect and for parts of the survey there are considerable cable feathering problems.

550 Figure B1 illustrates the former problem and shows the cross-line shot position error as a
551 function of distance along the line. We observe a large deviation between 11.5 and 17 km, where
552 the actual cross-line offset is as high as up to 500 m. However, the typical error in the cross-line
553 direction is much less and generally less than 100 m. The cable feathering problem is illustrated
554 in Figure B2, which shows the cross-line offset distribution for the MY101 (1999) survey. The
555 D13(2011) survey has similar problems. As shown by Nedimovic et al (2013) cable feathering
556 can potentially cause unacceptable changes both in traveltime and amplitude unless taken into
557 account in the processing sequence. There are also differences between the two surveys in the
558 cable length and cable depths causing further complications for the processing of the two
559 surveys.

560

561 It is clear that we cannot expect to produce accurate time-lapse amplitude maps of the type
562 routinely produced in conjunction with hydrocarbon exploration (Landrø, 1999). However, by
563 reducing ambitions and concentrate on the travel time differences between the two datasets we
564 should still be able to extract meaningful information about the subsurface. A mitigating
565 circumstance is the fact that the cross-line dip in the area is quite small, reducing the impact on
566 travel times from errors in the source-receiver positions.

567

568 The processing sequence can be summarized as:

569

- 570 1. Interpolation of shots to a nominal geometry
- 571 2. Shot designation
- 572 3. Matching of the MY101 (1999) and D13 (2011) surveys at the shot level.
- 573 4. Velocity analysis
- 574 5. Kirchhoff prestack time migration
- 575 6. Final output

576

577 The first step of the processing sequence was designed to minimize the impact of cable
578 feathering and differences in source-receiver geometry between the two surveys. In principle a
579 2D seismic line with significant cable feathering must be processed as if it were a 3D shot line.
580 The most straightforward approach is to use a 3D interpolation scheme taking the true 3D
581 receiver and source geometry into account and outputting interpolated data along the 2D survey
582 line. We use a version of Shepard's algorithm (Shepard, 1968) to perform the interpolation.
583 Before interpolation the input data is NMO-corrected with the water velocity. The NMO-
584 correction is backed off after interpolation. This compensates somewhat for offset errors and
585 increases the accuracy of the interpolated data.

586

587 To verify the interpolation we simulated the 1999 survey using the true source-receiver positions
 588 with a 3D finite-difference modeling program. The velocity model was constructed using
 589 bathymetry data from the area around the survey line. The synthetic data was then prestack time
 590 migrated and the travel time error was measured from the migrated sections. Figure B3 shows
 591 that the time shift error is close to 2 ms for most of the survey, except for two specific areas
 592 where it reaches 8 ms.

593

594 Designature of the shots were performed to remove the effect of the air gun bubble. A synthetic
 595 dataset was simulated using a point source in a half-space with a free surface. This was used as
 596 the desired wavelet in a 2D F-K deconvolution approach to produce a debubble filter. Figure B4
 597 shows an example of the input and desired output. The final filter used was taken as the average
 598 of a number of filters to avoid overfitting. Figure B5 shows an example of the application of the
 599 filter to a shot record.

600

601 After interpolation of shot records and debubble a single global match filter was designed to
 602 match the MY101 (1999) dataset to the D13 (2011) data. The global match filter was based on an
 603 average of individual match filters for all shots. The match filter is shown in figure B6 and
 604 Figure B7 shows an example of the application of the filter.

605

606 A standard velocity analysis with autopicking (see appendix C) was used to derive velocity
 607 models for the the two datasets. A smoothing filter with an aperture of 500 m was used for
 608 smoothing of the velocity field.

609

610 Kirchhoff prestack time-migration using a straight-ray approximation was used to produce the
 611 final migrated sections. The resolution of the migration is approximately proportional to the
 612 square of the homogeneous Green's function (Thorbecke and Wapenaar, 2007)

613

$$614 \quad \Gamma(r, \omega) \sim \frac{\sin(kr)}{2\pi r} \quad (\text{B1})$$

615

616 Where $k = \omega/c$, ω is the angular frequency, c is the velocity and r is the distance from the
 617 image point. For a frequency of 20 Hz, and a velocity of 2000 m/s the area contributing to an
 618 image point has a diameter of approximately 100 m.

619

620 ***The effect of of cross-line dip and cable feathering on zero-offset traveltime***

621

622 In the following we consider only the MY101 (1999) survey, since the errors for the D13 (2011)
 623 survey are in general less than the 1999 survey.

624

625 For our analysis the most critical errors due to inaccurate source and receiver positions are the
 626 travel time errors. The travel time τ for a dipping reflector is given by

627

$$628 \quad \tau = \sqrt{\tau_0^2 + \frac{h^2}{V_{nmo}^2}} \quad (\text{B2})$$

629

630 where τ_0 is the zero-offset travel time, h is the offset and V_{nmo} is the dip-dependent apparent
 631 stacking velocity (Levin, 1971). The zero offset travel time is measured along a ray path normal
 to the dipping layer and will depend on the midpoint-position. The stacking velocity depends on

632 the dip angle of the reflector and the direction of the survey line. Figure B8 shows the depth of
 633 the seafloor in an area around the survey line. The local dip angles in the in-line and cross-line
 634 direction are quite small, less than 10 degrees, and we can safely ignore the dip dependence and
 635 assume that V_{nmo} is the same as the stacking velocity for a plane reflector (Levin, 1971).
 636 An error in the source and receiver position can be described by an error in the offset Δh and an
 637 error in the vertical travel time τ_0 . The travel time τ depends on the midpoint position only
 638 through the zero-offset travel time, hence we can describe the effect of errors in the midpoint
 639 position by the equivalent error in the zero-offset travel time.

640
 641 The error $\Delta\tau$ in the travel time are found by simple sensitivity analysis of equation B2 to be
 642

$$643 \quad \Delta\tau = \frac{\tau_0}{\tau} \Delta\tau_0 + \frac{h}{\tau V_{NMO}^2} \Delta h. \quad (B3)$$

644
 645 For the processing sequence we are using the zero-offset travel time is controlled by the near
 646 offsets. Any errors in the near-offset midpoints will induce errors in the zero-offset travel time
 647 due to the varying depth of the dipping reflector. Figure B9 shows the distribution of midpoint
 648 errors in the direction normal to the survey line. In the inline direction the error in the midpoint
 649 position will generally be less than half the receiver distance, which is equal to 12.5 m. The
 650 cross-line error is generally less than 100 m, which is within the lateral resolution limit of the
 651 prestack time migration.

652
 653 Figures B10 and B11 show the distributions of depth differences between the seafloor depth and
 654 lines centered on each shot point and extending 100 meters in the cross line direction and 25 m
 655 meters in the inline direction.

656
 657 From these figures a reasonable estimate of the depth differences in the inline and cross-line
 658 directions are 3 meters which combined would give an error of at most 6 m and an error in the
 659 zero-offset travel time of

$$660 \quad \Delta t_0 \leq 2 \left(\frac{6}{1500} \right) = 8 \text{ ms.}$$

662
 663 where we have used a stacking velocity equal to 1500 m/s. This is probably an upper limit, and a
 664 more reasonably combined depth difference of 4 m would give a zero-offset travel time error of
 665 5 ms.

666
 667 Figure B3 shows the cross-line offset distribution for all offsets. The maximum cross-line offset
 668 is about 1000 m, which occurs only for the largest offsets. For a travel time of 3 seconds,
 669 equation B3 gives a travel time error of approximately 32 ms at an offset of 3000 m. It is now
 670 important to understand that this travel time error does not show up directly in the final migrated
 671 sections. This travel time error is manifested as an error in the estimated stacking velocity since
 672 equation B1 shows that a change in offset is indistinguishable from a change in the stacking
 673 velocity and in fact an error in the stacking velocity ΔV_{NMO} gives an error in the travel time as

674
 675

676

$$\Delta\tau = -\frac{1}{\tau} \frac{h^2}{V_{NMO}^3} \Delta V_{NMO} \quad (\text{B4})$$

677

678 Using equation (B4) an error in the travel time of 32 ms corresponds to an error of approximately
679 40 m/s in the stacking velocity. In the final seismic image this will appear as a slight error in the
680 amplitude, the image being slightly defocused. The vertical travel time measured from the
681 seismic section will only be affected by the depth differences due to the error in the near offset
682 midpoints.

683

684 We can conclude that the errors in the source and receiver positions will at most imply an error
685 in the zero-offset two-way travel time measured on the seismic section of 8 ms, but more likely
686 is an error of 5 ms. These estimates are in accordance with the results shown in Figure B3.

687

688 **Appendix C: Seismic velocity field within sediments**

689 The stacking velocities were estimated using an automatic method suggested by *Fomel (2009)*.
690 Figure C1 shows the estimated P-wave velocities before and after the earthquake for the upper
691 sediment layers only. The auto-picked velocities were deemed reliable above the basement
692 reflection only. Beneath the basement reflection, the auto picked velocities were deemed as
693 highly uncertain. This is due to the low signal to noise ratios and to the poorly resolved
694 semblance panels for these areas. A manual picking effort has also been carried out for picking
695 the stacking velocities beneath the basement, however for the offset ranges considered in this
696 data the velocities are poorly resolved. Hence, we have chosen to mute the velocities beneath the
697 basement in Figure C1. The muted velocities have no influence on the results of this work, as
698 only the upper sediment reflections were used in the analysis. It is interesting to observe the
699 increase of high velocities (yellow color) between 50 and 65 km, close to the trench axis. One
700 potential interpretation is that the sediments in this region have been compressed due to an
701 upward force acting towards East and the trench axis.

702

703 **Appendix D: Geomechanical modeling**

704

705 *Geertsmaa (1973)* derived a simple model for geomechanics, the nucleus of strain model. *Fjær et*
706 *al. (2008)*, gives a simplified approximation of the vertical displacement (u_z) along the center line
707 above a compacting reservoir:

708

$$u_z = -H_0 \left[3 - 4\nu + \frac{d-z}{|d-z|} - \frac{d-z}{\sqrt{r^2 + (d-z)^2}} - \frac{(d+z)(3-4\nu)}{\sqrt{r^2 + (d+z)^2}} + \frac{2r^2 z}{(r^2 + (d+z)^2)^{\frac{3}{2}}} \right], \quad (\text{D1})$$

709

710 where ν is the Poisson ratio for the elastic rock, d is the depth of the compacting reservoir, z is
711 the distance from the surface and r is the radius of the reservoir. H_0 is dependent on several rock
712 physics parameters, among them the pore pressure change causing the compaction. However, for
713 our purpose the details of this constant is not crucial, and we will treat this H_0 as an empirical
714 fitting factor in our simple simulations. One example of such a modelling is shown in Figure D1,
715 assuming reservoir radii of 2 and 3 km, respectively. From such modeling we can estimate the
716 stretch within the sedimentary unit. For a 2 km radius we observe that the overburden stretch is
717 approximately 5-6 m, and that it is reduced to 3-4 m for a radius of 3 km. This modeling is very
718 similar to observations from the Ekofisk reservoir in the North Sea, where the seabed subsidence

719 is up to 9 m caused by the compaction of the chalk reservoir at 3 km depth. Once the stretch is
 720 known, we can estimate dz/z and hence we can estimate the R -factor from equation 3, since the
 721 relative timeshift within the sedimentary layer is known from the time-lapse seismic data. We
 722 found an “average” R -factor of approximately 7 that is assumed constant for the first 20 km
 723 along the 2D seismic profile. This number is of course very uncertain, since we do not know the
 724 radius of the rock units that we assume has been subsiding at the sediment-basement interface.
 725 However, this number is in agreement with Hatchell and Bourne (2005) where an overburden R -
 726 value of 5 was used.

727

728 **Acknowledgments**

729 The Norwegian Research Council is acknowledged for financial support (Grant 228400). A part
 730 of this study was supported by KAKENHI Grants-in-Aid for Specially Promoted Research,
 731 number JP26000002, and for Scientific Research (S), number JP15H05718, from the Japan
 732 Society for the Promotion of Science. Raw seismic data are available from authors upon request.

733

734 **References**

- 735 Amundsen, L. and Landrø, M., 2010. Marine Seismic Sources, Part 1: Air-guns for non experts,
 736 *GeoExpro*, 7, No. 2, 32-35.
- 737
 738 Arts, R., Chadwick, A., Eiken, O., Thibeau, S. and Nooner, S., 2008. Ten years' experience of
 739 monitoring CO₂ injection in the Utsira sand at Sleipner, offshore Norway, *First Break*, 26, 65-72.
- 740
 741 Barkved, O. I. and Kristiansen, T., 2005. Seismic time-lapse effects and stress changes:
 742 Examples from a compacting reservoir, *The Leading Edge*, 24, 1244-1248.
- 743
 744 Bathija, A. P., Batzle, M. and Prasad, M., 2009. An experimental study of the dilation factor,
 745 *Geophysics*, 74, E181-E191.
- 746
 747 Bergman, P., Yang, C., Lüth, S., Juhlin, C., Cosma, C., 2011. Time-lapse processing of 2D
 748 seismic profiles with testing of static correction methods at the CO₂ injection site Ketzin
 749 (Germany), *Journal of Applied Geophysics*, 75, 124-139.
- 750
 751 Chen, C-T. and Millero, F.J., 1977. Speed of sound in seawater at high pressures, *J. Acoust. Sos.*
 752 *Am.*, 62, 1129-1135.
- 753
 754 Chester, F. M., Rowe, C., Ujiie, K., Kirkpatrick, J., Regalla, C., Remitti, F., Moore, J. C., Toy,
 755 V., Wolfson-Schwehr, M., Bose, S., Kameda, J, Mori, J. J., Brodsky, E. E., Eguchi, N., Toczko,
 756 S., Expedition 343 and 343T Scientists, 2013. Structure and composition of the plate-boundary
 757 slip zone for the 2011 Tohoku-Oki earthquake. *Science*, v. 342(6163), 1208-1211.
- 758
 759 Chu, R., Wei, S., Helmberger, D.V., Zhan, Z, Zhu, L., Kanamori, H., 2011. Initiation of the great
 760 Mw 9.0 Tohoku-Oki earthquake, *Earth and Planetary Science Letters*, 308, 277-283.

- 761
762 Eiken, O. and Tøndel, R., 2005. Sensitivity of time-lapse seismic data to pore pressure changes:
763 Is quantification possible?, *The Leading Edge*, 24, 1250-1254.
764
- 765 Fofonoff, N. P. and Millard Jr., R.C., 1983. Algorithms for computation of fundamental
766 properties of seawater, *UNESCO technical papers in marine science*, 44.
767
- 768 Fujii, Y., Satake, K., Sakai, S. I., Shinohara, M., and Kanazawa, T., 2011. Tsunami source of the
769 2011 off the Pacific coast of Tohoku Earthquake. *Earth, planets and space*, v. 63(7), 815.
770
- 771 Fujiwara, T., Kodaira, S., No, T., Kaiho, Y., Takahashi, N. and Kaneda, Y., 2011. The 2011
772 Tohoku-Oki earthquake: Displacement reaching the trench axis. *Science*, v. 334(6060), 1240-
773 1240.
774
- 775 Fjær, E., Holt, R.M., Horsrud, P., Raaen, A.M. and Risnes, R., 2008. Petroleum related rock
776 mechanics, *Developments in Petroleum Science 53*, Elsevier, 2nd edition, ISBN: 978-0-444-
777 50260-5.
778
- 779 Fomel, S., 2009. Velocity analysis using *AB* semblance. *Geophysical Prospecting*, 57, 311–321.
780 doi:10.1111/j.1365-2478.2008.00741.x.
781
- 782 Geertsma, J., 1973. A basic theory of subsidence due to reservoir compaction: The
783 heterogeneous case, *Verhandelingen Kon. Ned. Geol. Mijnbouwk. Gen*, 28, 43-62.
784
- 785 Guilbot, J. and Smith, B., 2002. 4-D constrained depth conversion for reservoir compaction
786 estimation: Application to Ekofisk Field, *The Leading Edge*, 21, 302-308.
787
- 788 Hatchell, P. J., Kawar, R.S., and Savitski, A.A., 2005. Integrating 4D seismic, geomechanics and
789 reservoir simulation in the Valhall oil field: *67th Conference and Exhibition, EAGE, Extended*
790 *Abstracts*, C012.
791
- 792 Hatchell, P. and Bourne, S., 2005. Rocks under strain: Strain-induced time-lapse time shifts are
793 observed for depleting reservoirs, *The Leading Edge*, 24, 1222-1225.
794
- 795 Ide, S., Baltay, A., and Beroza, G. C., 2011. Shallow dynamic overshoot and energetic deep
796 rupture in the 2011 Mw 9.0 Tohoku-Oki earthquake. *Science*, v. 332(6036), 1426-1429.
797
- 798 IPCC, 2005, Special Report on Carbon Dioxide Capture and Storage, edited by Metz, B.,
799 Davidson, O., de Coninck, H., Loos M. and Meyer, L., *Cambridge University Press*, ISBN-13
800 978-0-521-86643-9.
801
- 802 Ito, Y., Tsuji, T., Osada, Y., Kido, M., Inazu, D., Hayashi, Y., Tsushima, H., Hino, R. and
803 Fujimoto, H., 2011. Frontal wedge deformation near the source region of the 2011 Tohoku-Oki
804 earthquake, *Geophys. Res. Lett.*, 38. L00G05, doi: 10.1029/2011GL048355.
805

- 806 Jiang, J. and Simons, M., 2016. Probabilistic imaging of tsunamigenic seafloor deformation
807 during the 2011 Tohoku-oki earthquake, *J. Geophys. Res. Solid Earth*, *121*, 9050-9076,
808 doi:10.1002/2016JB013760.
- 809
810 Jolivet L., and Tamaki, K., 1992. Neogene kinematics in the Japan region and volcanic activity
811 of the northeast Japan arc, *Proc. Ocean Drill. Program Sci. Results*, v. *127/128*, Part 2, p. 1311-
812 1331.
- 813
814 Juanes, R, H., Hager, B.H. and Herzog, H.J., 2012. No geologic evidence that seismicity causes
815 fault leakage that would render large-scale carbon capture and storage unsuccessful, *PNAS*, *109*,
816 E3623.
- 817
818 Kido, M., Osada, Y., Fujimoto, H., Hino, R. and Ito, Y., 2011. Trench-normal variation in
819 observed seafloor displacements associated with the 2011 Tohoku-Oki earthquake. *Geophysical*
820 *Research Letters*, *38*(24).
- 821
822 Kodaira, S., No, T., Nakamura, Y., Fujiwara, T., Kaiho, Y., Miura, S., Takahashi, N., Kaneda, Y.
823 and Taira, A., 2012. *Nature Geoscience Letters*, DOI: 10.1038/NGEO1547.
- 824
825 Kodaira, S., Nakamura, Y., Yamamoto, Y., Obana, K., Fujie, G., No, T., Kaiho, Y., Sato, T. and
826 Miura, S., 2017. Depth-varying structural characters in the rupture zone of the 2011 Tohoku-oki
827 earthquake. *Geosphere*, DOI:doi.org/10.1130/GES01489.1
- 828
829 Landrø, M., 1999. Repeatability issues of 3D VSP data, *Geophysics*, *64*, 1673-1679.
- 830
831 Landrø, M., Solheim, O.A., Hilde, E., Ekren, B.O. and Strønen, L.K., 1999. The Gullfaks 4D
832 study. *Petroleum Geoscience*, *5*, 213-226.
- 833
834 Landrø, M., 2001. Discrimination between pressure and fluid saturation changes from time lapse
835 seismic data, *Geophysics*, *66*, 836-844.
- 836
837 Landrø, M. and Stammeijer, J., 2004. Quantitative estimation of compaction and velocity
838 changes using 4D impedance and travelttime changes, *Geophysics*, *69*, 949-957.
- 839
840 Landrø, M., 2011. Seismic monitoring of an old underground blowout – 20 years later, *First*
841 *Break* *29*, 39-48
- 842
843 Landrø, M., 2015. *Petroleum Geoscience*, edited by K. Bjørlykke, Chapter 19, pp 489-514,
844 *Springer*, 2nd edition, DOI 10.1007/978-3-642-34132-8.
- 845
846 Landrø, M. and Zumberge, M., 2017. Estimating saturation and density changes caused by CO₂
847 injection at Sleipner – Using time-lapse seismic amplitude-variation-with-offset and time-lapse
848 gravity, *Interpretation*, *5*, T243-T257.
- 849

- 850 Lay, T., Ammon, C. J., Kanamori, H., Xue, L., and Kim, M. J., 2011. Possible large near-trench
851 slip during the 2011 Mw 9.0 off the Pacific coast of Tohoku Earthquake. *Earth, planets and*
852 *space*, v. 63(7), p. 687-692.
- 853
854 Lee, W.H.K. and Cox, C.S., 1966. Time variation of ocean temperatures and its relation to
855 internal waves and oceanic heat flow measurements, *Journal of Geophysical Research*, 71, 2101-
856 2111.
- 857
858 Levin, F. K., 1971. Apparent velocity from dipping interface reflections, *Geophysics*, 36, 510-
859 516.
- 860
861 Mackenzie, K. V., 1981. Nine-term equation for sound speed in the oceans, *J. Acoust. Soc. Am.*,
862 70, 807-812.
- 863
864 Nedimovic, M. R. and West, G. F., 2003, Crooked-line 2D seismic reflection imaging in
865 crystalline terrains: Part 1, data processing, *Geophysics*, 68, 274-285.
- 866
867 Osdal, B. and Landrø, M., 2011. Estimation of changes in water column velocities and
868 thicknesses from time lapse seismic data, *Geophysical Prospecting*, 59, 295-309.
- 869
870 Røste, T., Stovas, A., and Landrø, M., 2005. Estimation of layer thickness and velocity changes
871 using 4D prestack seismic data: 67th Conference and Exhibition, EAGE, Extended Abstracts,
872 CO10.
- 873
874 Røste, T., Landrø, M. and Hatchell, P., 2007. Monitoring overburden layer changes and fault
875 movements from time-lapse seismic data on the Valhall Field, *Geophys. J. Int.*, 170, 1100-1118.
- 876
877 Røste, T., Dybvik, O.P. and Søreide, O.K., 2015. Overburden 4D time shifts induced by
878 reservoir compaction at Snorre field, *The Leading Edge*, 34, 1366–1374.
879 doi: 10.1190/tle34111366.1
- 880
881 Satake, K., Fujii, Y., Harada, T. and Namegaya, Y., 2013. Time and space distribution of
882 coseismic slip of the 2011 Tohoku earthquake as inferred from tsunami waveform data. *Bulletin*
883 *of the Seismological Society of America*, v. 103(2B), 1473-1492.
- 884
885 Sato, M, Ishikawa, T., Ujihara, N., Yoshida, S., Fujita, M., Mochizuki, M. and Asada, A., 2011.
886 Displacement above the hypocenter of the 2011 Tohoku-Oki earthquake, *Science*, 332,
887 1395.
- 888
889 Shepard, D., 1968. A two-dimensional interpolation function for irregularly-spaced
890 data". *Proceedings of the 1968 ACM National Conference*. pp. 517–524.
- 891
892 Tamaki, K., Pisciotto, K. and Allan, J., 1990. *Proc. Ocean Drill. Program Initial Rep.* 127, 4.
893

- 894 Tanaka, Y., Sawada, Y., Tanase, D., Tanaka, J., Shiomi, S. and Kasukawa, T., 2017. Tomakomai
895 CCS demonstration project of Japan, CO₂ injection in process, *Energy Procedia*, 114, 5836-
896 5846.
- 897
898 Tsuji, T., Matsuoka, T., Kadir, W.G.A., Hato, M., Takahashi, T., Sule, M.R., Kitamura, K.,
899 Yamada, Y., Onishi, K., Widarto, D.S., Sebayang, R.I., Prasetyo, A., Priyono, A., Ariadji, T.,
900 Sapiie, B., Widiyanto, E., Asikin, A.R. and Gundih CCS project team, 2014. Reservoir
901 characterization for site selection in the Gundih CCS project, Indonesia, *Energy Procedia*, 63,
902 6335-6343.
- 903
904 Tsuru, T., Park, J-O., Takahashi, N., Kodaira, S., Kido, Y., Kaneda, Y. and Kono, Y., 2000.
905 Tectonic features of the Japan Trench convergent margin off Sanriku, northeastern Japan
906 revealed by multi-channel seismic reflection data, *J. Geophys. Res.*, 105, 16,403-16,413.
- 907
908 Tsuru, T., Park, J-O., Miura, S., Kodaira, S., Kido, Y. and Hayashi, T., 2002. Along-arc
909 structural variation of the plate boundary at the Japan Trench margin: Implication of interpolate
910 coupling, *Journal of Geophysical Research*, 107, 2357.
- 911
912 Thorbecke, J. and Wapenaar, K., 2007. On the relation between seismic interferometry and the
913 migration resolution function, *Geophysics*, 72, T61-T66.
- 914
915 von Huene, R., and Culotta, R., 1989. Tectonic erosion at the front of the Japan Trench
916 convergent margin. *Tectonophysics*, v. 160(1-4), 75-90.
- 917
918 von Huene, R., and Lallemand, S., 1990. Tectonic erosion along the Japan and Peru convergent
919 margins. *Geological Society of America Bulletin*, v. 102(6), 704-720.
- 920
921 von Huene, R., Klaeschen, D., Cropp, B., and Miller, J., 1994. Tectonic structure across the
922 accretionary and erosional parts of the Japan Trench margin. *Journal of Geophysical Research:*
923 *Solid Earth*, v. 99(B11), 22349-22361.
- 924
925 Verdon, J. P., 2014. Significance for secure CO₂ storage of earthquakes induced by fluid
926 injection, *Environmental Research Letters*, 9, 064022 (10 pp).
- 927
928 Weibull, W. W. and Arntsen, B., 2013. Automatic velocity analysis with reverse-time migration,
929 *Geophysics*, 78, S179-S192.
- 930
931 Wong, G. S. K. and Zhu, S., 1995. Speed of sound in seawater as a function of salinity,
932 temperature and pressure, *J. Acoust. Soc. Am.*, 97, 1732-1736.
- 933
934 Zadeh, M. H. and Landrø, M., 2011. Monitoring a shallow subsurface gas flow by time lapse
935 refraction analysis, *Geophysics*, 76, O35-O43.
- 936
937 Zoback, M. D. and Gorelick, S.M., 2012. Earthquake triggering and large-scale geologic storage
938 of carbon dioxide, *PNAS*, 109, 10164-10168.
- 939
940

941
942
943
944

TABLES

Source	Airgun 9000 cu.in
Source depth	10 m
Shotpoint interval	50 m
Streamer depth	15 m
Receiver interval	25 m
Maximum offset	3445 m
Low pass cutoff	3 Hz
High pass cutoff	102 Hz
Time sampling interval	4 ms
Record length	13.5 s

945
946
947
948
949
950
951

Table 1: Acquisition parameters for the MY101 (1999) survey.

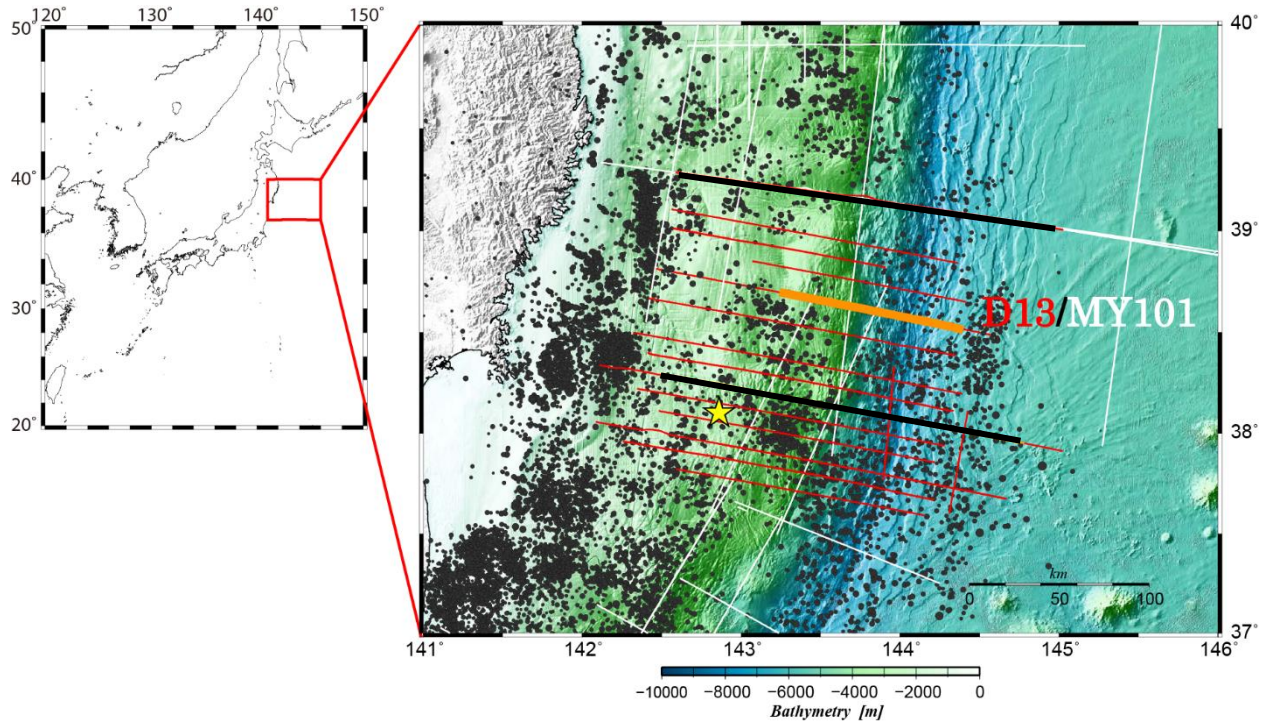
Source	Airgun 7800 cu.in
Source depth	10 m
Shotpoint interval	50 m
Streamer depth	21 m
Receiver interval	12.5 m
Maximum offset	5415 m
Low pass cutoff	3 Hz
High pass cutoff	200 Hz
Time sampling interval	2 ms
Record length	18 s

952
953
954
955
956
957
958
959
960
961
962
963
964
965
966
967
968
969
970
971

Table 2: Acquisition parameters for the D13 (2011) survey.

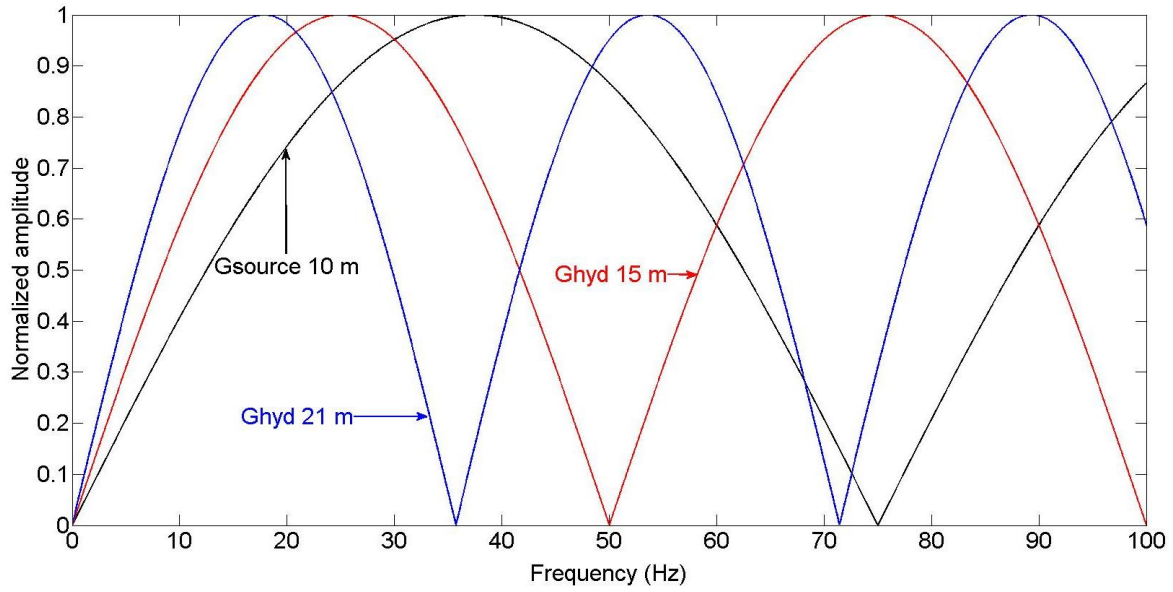
972
973
974
975
976
977

FIGURES



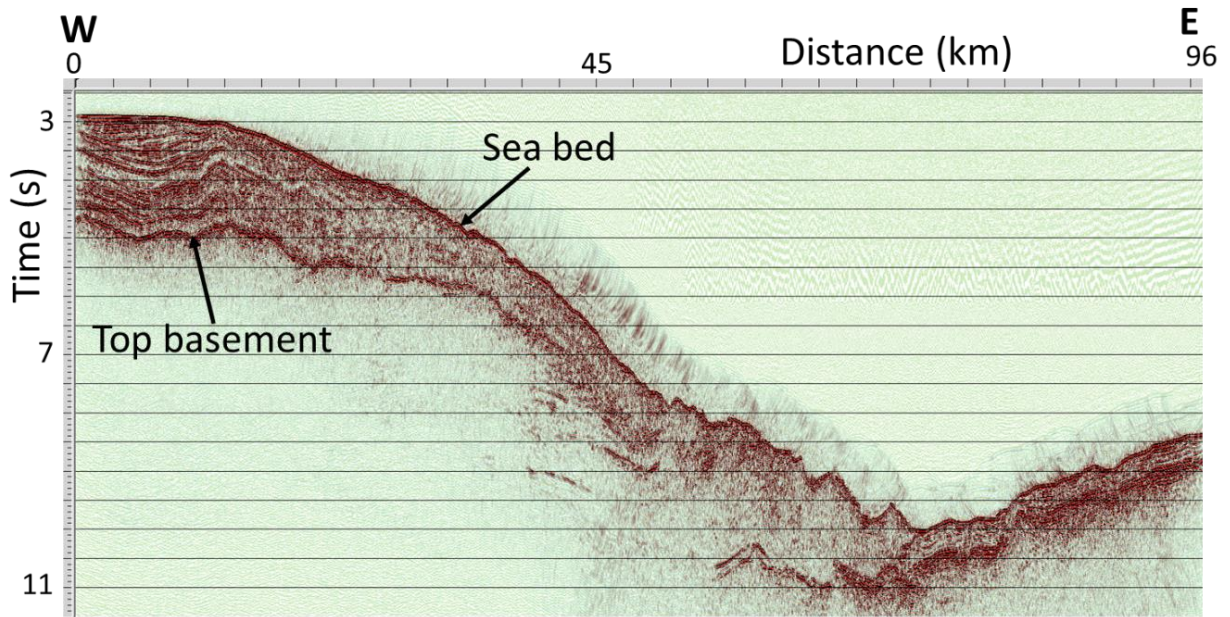
978
979
980
981
982
983
984
985
986
987
988
989
990

Figure 1. Bathymetric map of the Japan trench showing the 2D seismic line (solid orange line) used in this study (D13/MY101) and two additional lines (solid black lines) that have also been repeated but not used in this study. The yellow star indicates the epicentre for the Tohoku-Oku 2011 earthquake.



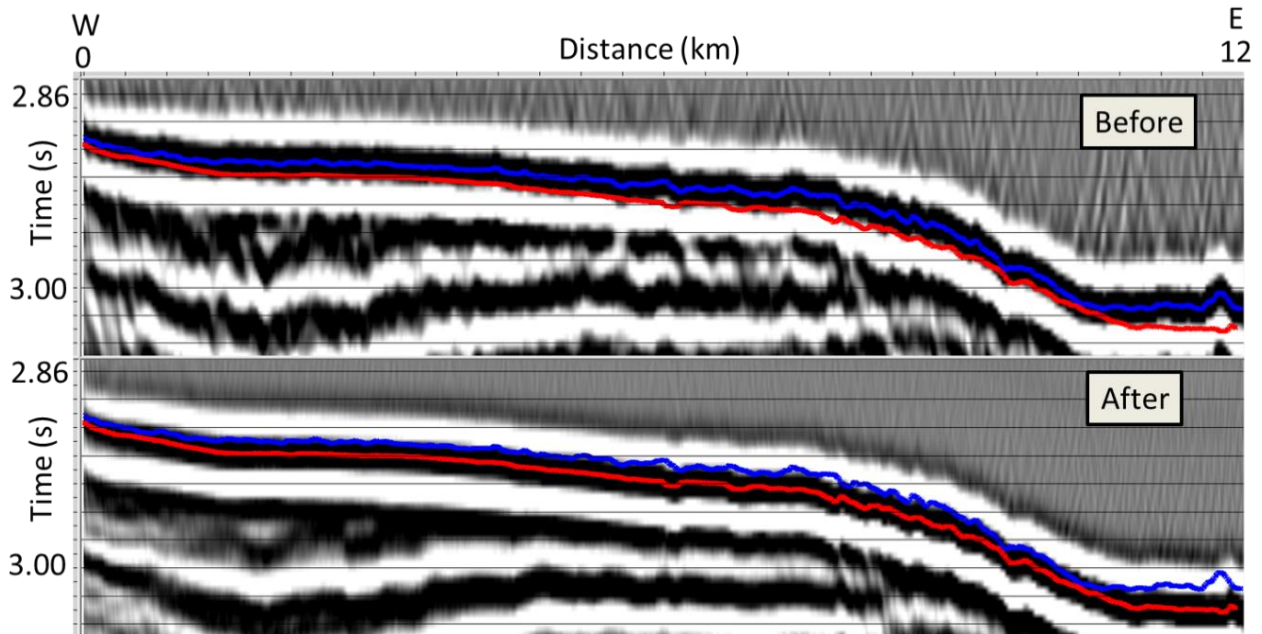
991
992
993
994
995
996
997
998
999

Figure 2. Normalized source (black line) and receiver ghost spectra (red line for 15 m receiver depth and blue line for 21 m received depth). Notice that the 2011 data will have limited amount of data around 36 Hz and the 1999 data will have a similar loss of data around 50 Hz.



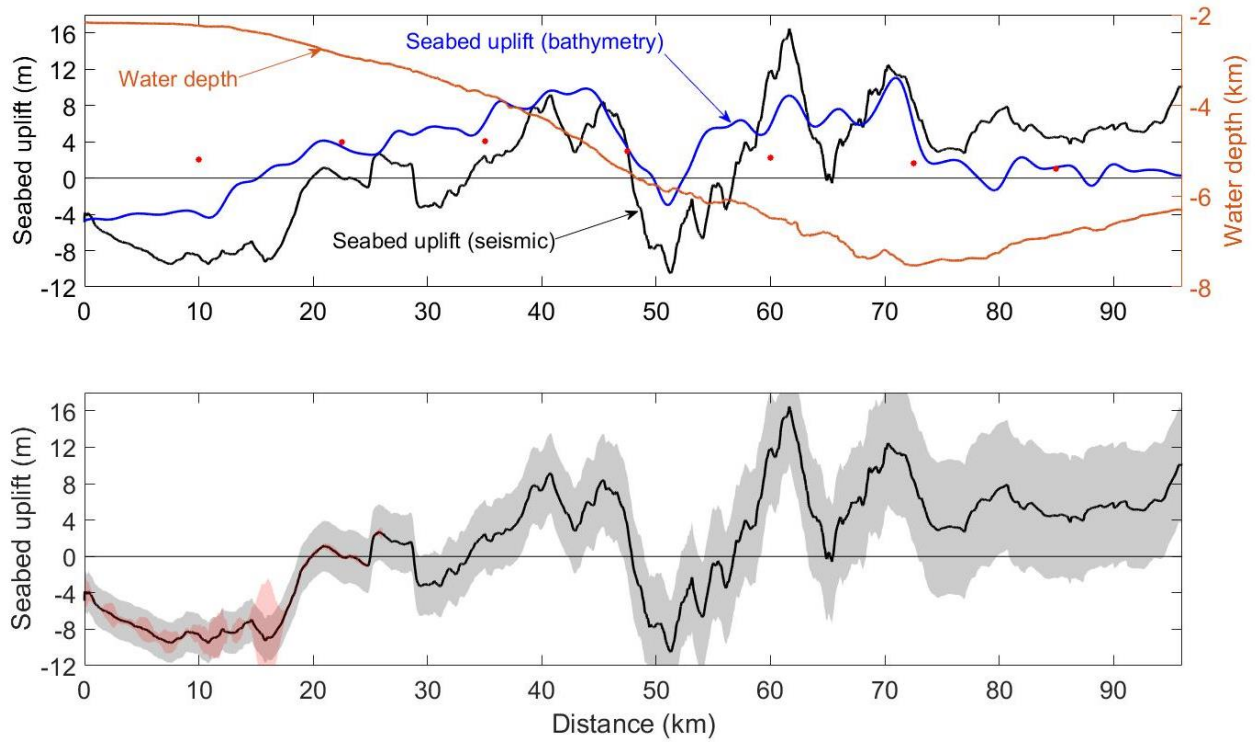
1000
1001
1002
1003
1004

Figure 3. The seismic 2D line (before the earthquake).



1005
 1006
 1007
 1008
 1009
 1010
 1011
 1012
 1013
 1014
 1015
 1016
 1017

Figure 4. The vertical movement of the seabed observed on the time lapse seismic data before (top) and after (bottom) the earthquake. The blue line represents the maximum peak pick before and the red line after. The average time shift is approximately 10 ms. Note that blue and red lines are plotted at the same positions in both sections, to clearly visualize the seismic travelttime shift between the two surveys for the seabed reflection.



1018
 1019 **Figure 5.** Top: comparison between vertical seabed displacements estimated from bathymetric
 1020 data (blue) and the time lapse seismic data (black). The seabed profile is the brown curve and the
 1021 filled red circles are values taken from Figure 6d in Jiang and Simons paper from 2016. Bottom:
 1022 The estimated seismic displacements (black curve) and two types of uncertainty estimates shown
 1023 as shaded fill. The grey shaded area represent a systematic water velocity change of plus or
 1024 minus 1.5 m/s between the two seismic surveys, and the red shaded area represents errors
 1025 estimated from 3D modeling of shot position errors and the seabed topography (see Appendix
 1026 B).

1027
 1028
 1029
 1030
 1031
 1032
 1033
 1034
 1035
 1036
 1037
 1038
 1039
 1040
 1041
 1042
 1043

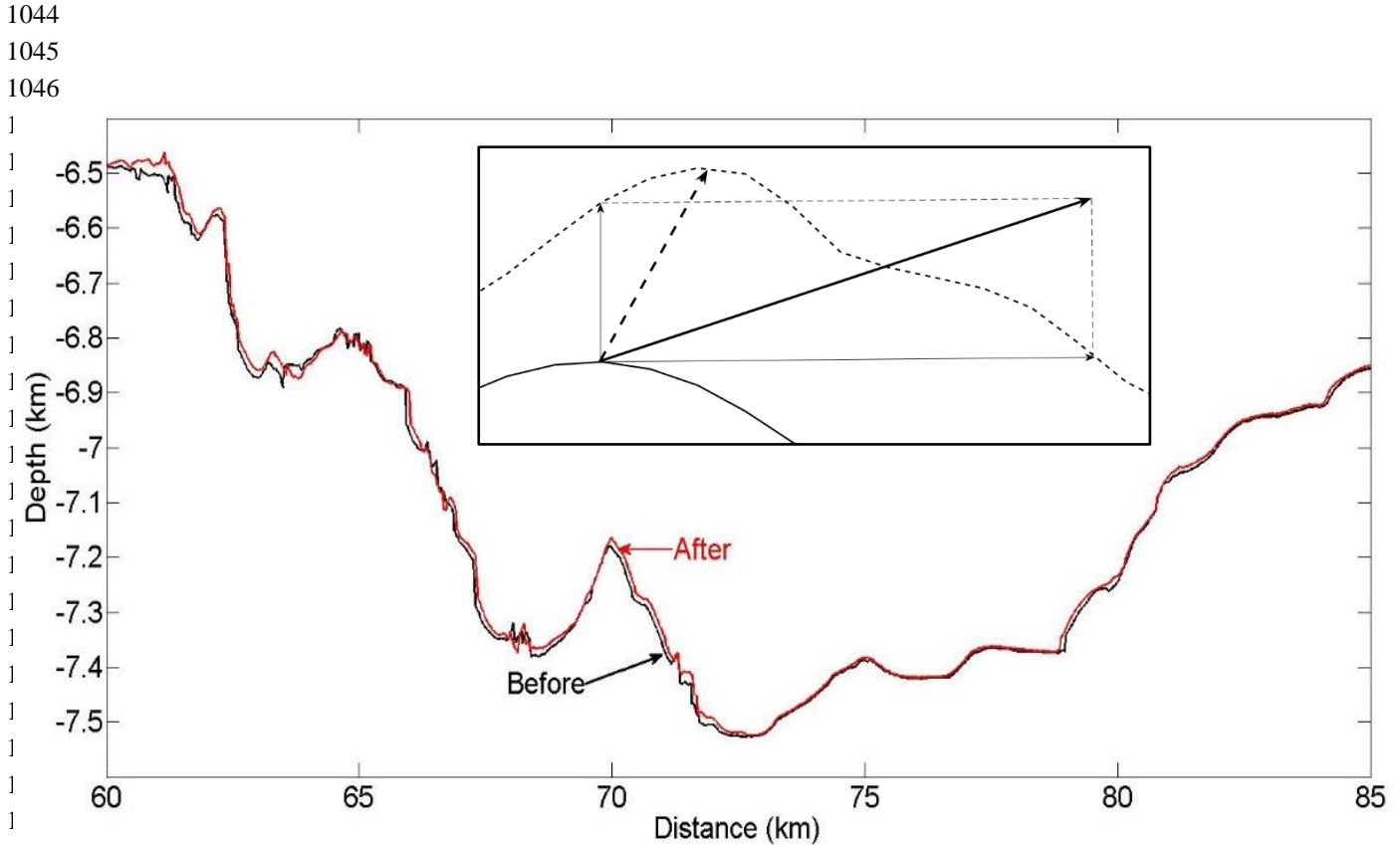
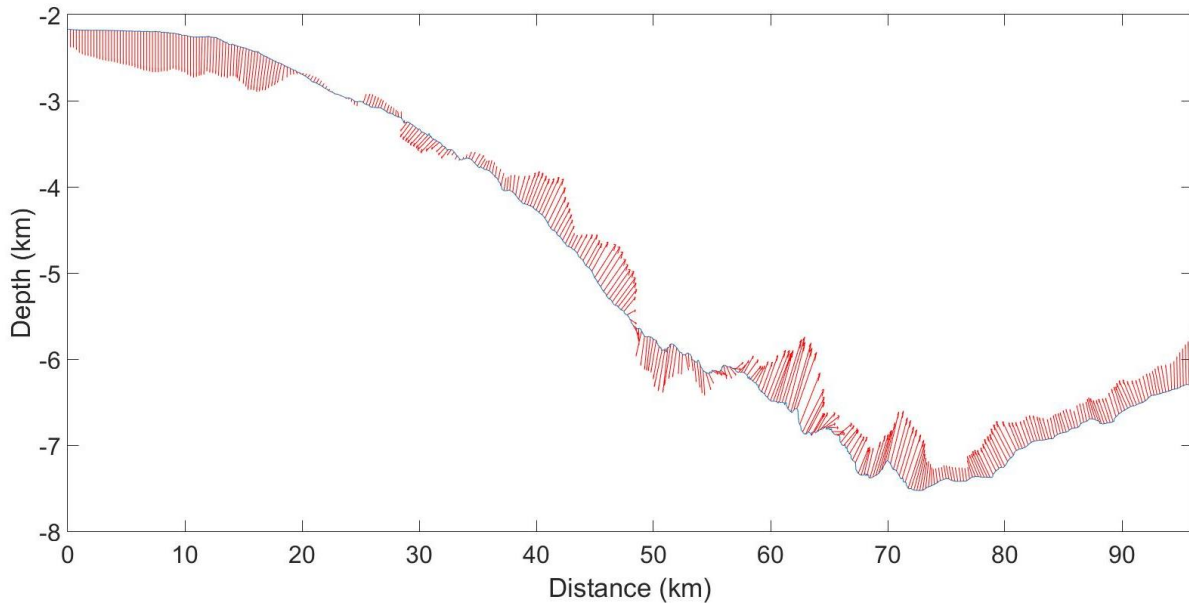
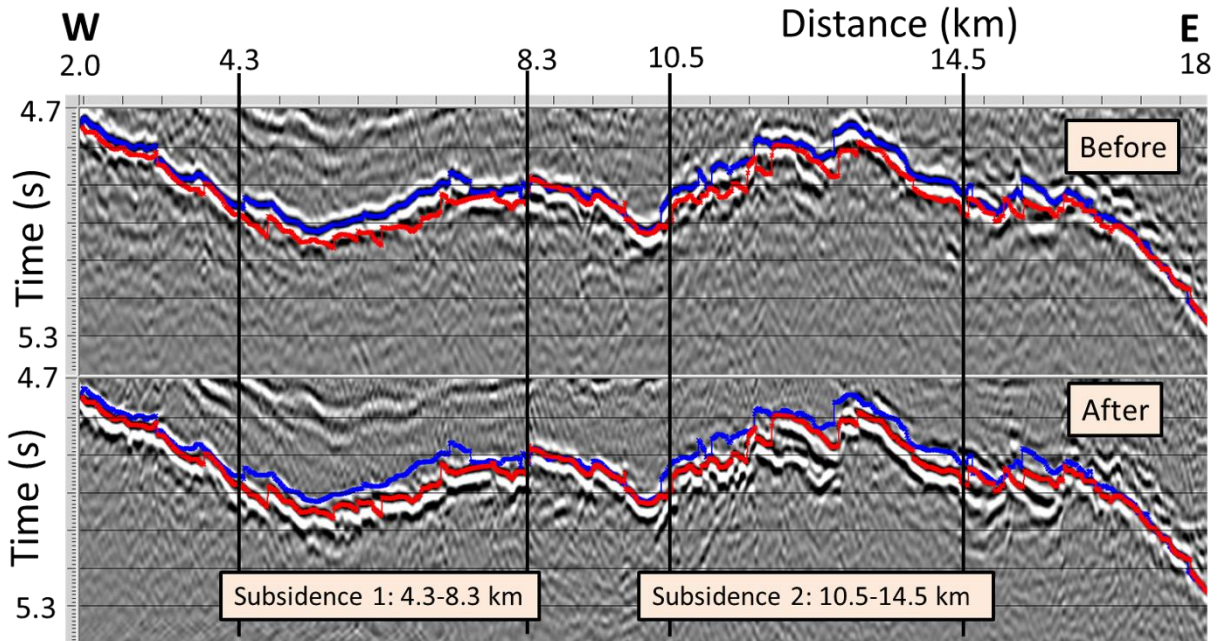


Figure 6. Estimated water depth based on automatic picking of the seabed reflection in time, assuming a constant water velocity of 1500 m/s. Notice the horizontal shift of approximately +60 m in the region between 60 and 70 km, and -40 m in the region between 78 and 85 km. Inserted: example showing the error introduced by the simple vector computation of displacement (solid arrow) versus the most likely one (dashed arrow). The solid and dashed curves in the inset represent the seabed position before and after the earthquake, respectively.



1074
1075
1076
1077
1078

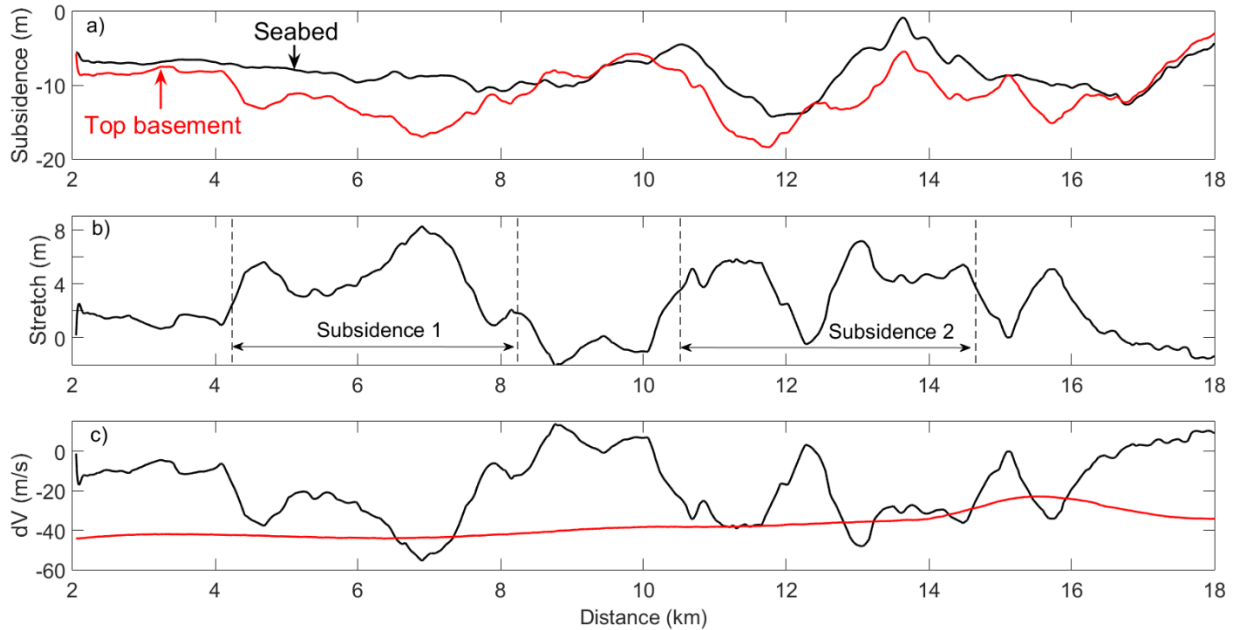
Figure 7. Estimated seabed displacement vectors (red arrows). Note that the vertical scale is exaggerated, so that the angles of the displacement vectors appear more vertical than they actually are. The displacement vectors have been multiplied by 50 for visualization purposes.



1079
1080
1081
1082
1083
1084
1085
1086

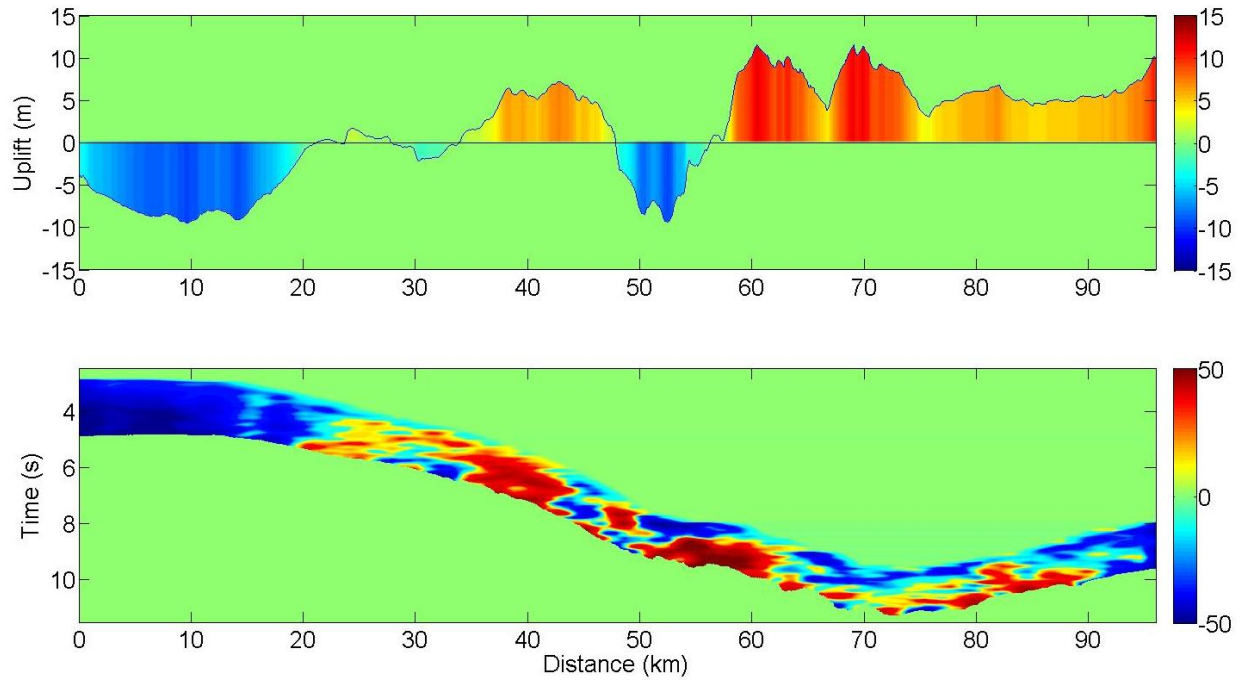
Figure 8a. Subsidence between 4 and 8.5 km and 10 and 16 km for the top basement. Blue and red lines show interpreted top basement before (top) and after (bottom) the earthquake. The top basement is first interpreted on the top figure as a blue solid line. Then this interpretation is copied to exactly the same position on the lower figure, then the top basement is interpreted on the lower figure as a red line, and copied into the upper figure. Notice the significant timeshift for the two subsidence zones, up to 50-60 ms.

1087
 1088
 1089
 1090
 1091
 1092
 1093
 1094
 1095



1096
 1097
 1098
 1099
 1100
 1101
 1102
 1103
 1104
 1105
 1106
 1107
 1108
 1109
 1110

Figure 9. a) Estimated subsidence at seabed (black solid line) and top basement (red solid line). b) Estimated stretch of the sediments, assuming an R -factor of 6.7. The two subsidence zones are indicated by dashed vertical lines. c) Comparison of velocity change estimates based on time lapse seismic timeshifts and assuming a constant R -factor of 6.7 (solid black line) and estimated average change in stacking velocities (red solid line). Notice that the two velocity change estimates show less deviation within the two subsidence zones.



1111
 1112
 1113
 1114
 1115
 1116
 1117
 1118
 1119
 1120
 1121
 1122
 1123
 1124
 1125
 1126
 1127
 1128
 1129
 1130
 1131
 1132
 1133
 1134
 1135
 1136
 1137
 1138

Figure 10. Estimated vertical uplift at seabed (top) and difference in estimated stacking velocities (bottom) from the time lapse seismic data. Notice dominantly increased velocities for the slope between 25 and 60 km. There is a good correlation between velocity changes and seabed uplift for the first 50 km, but less correlation for large water depths (between 50 and 96 km).

1139
 1140
 1141
 1142
 1143
 1144
 1145
 1146
 1147
 1148
 1149
 1150
 1151
 1152
 1153
 1154
 1155
 1156
 1157
 1158
 1159
 1160
 1161
 1162
 1163
 1164
 1165
 1166
 1167
 1168
 1169
 1170
 1171

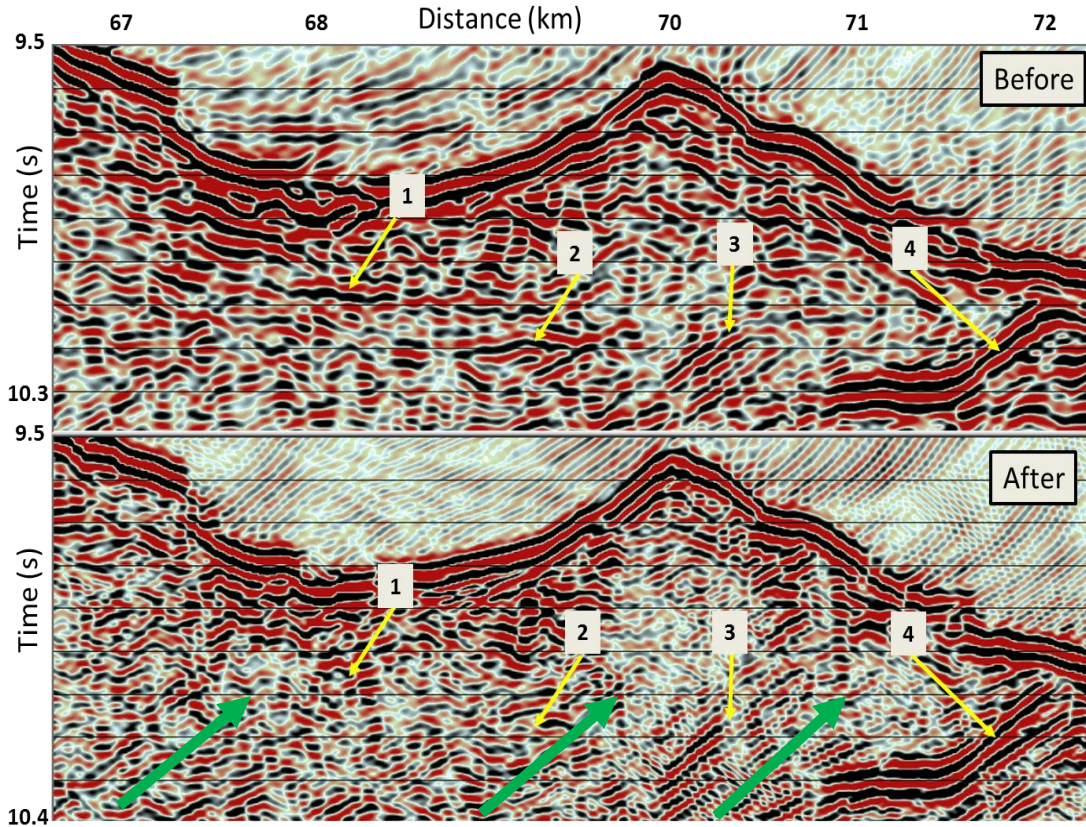
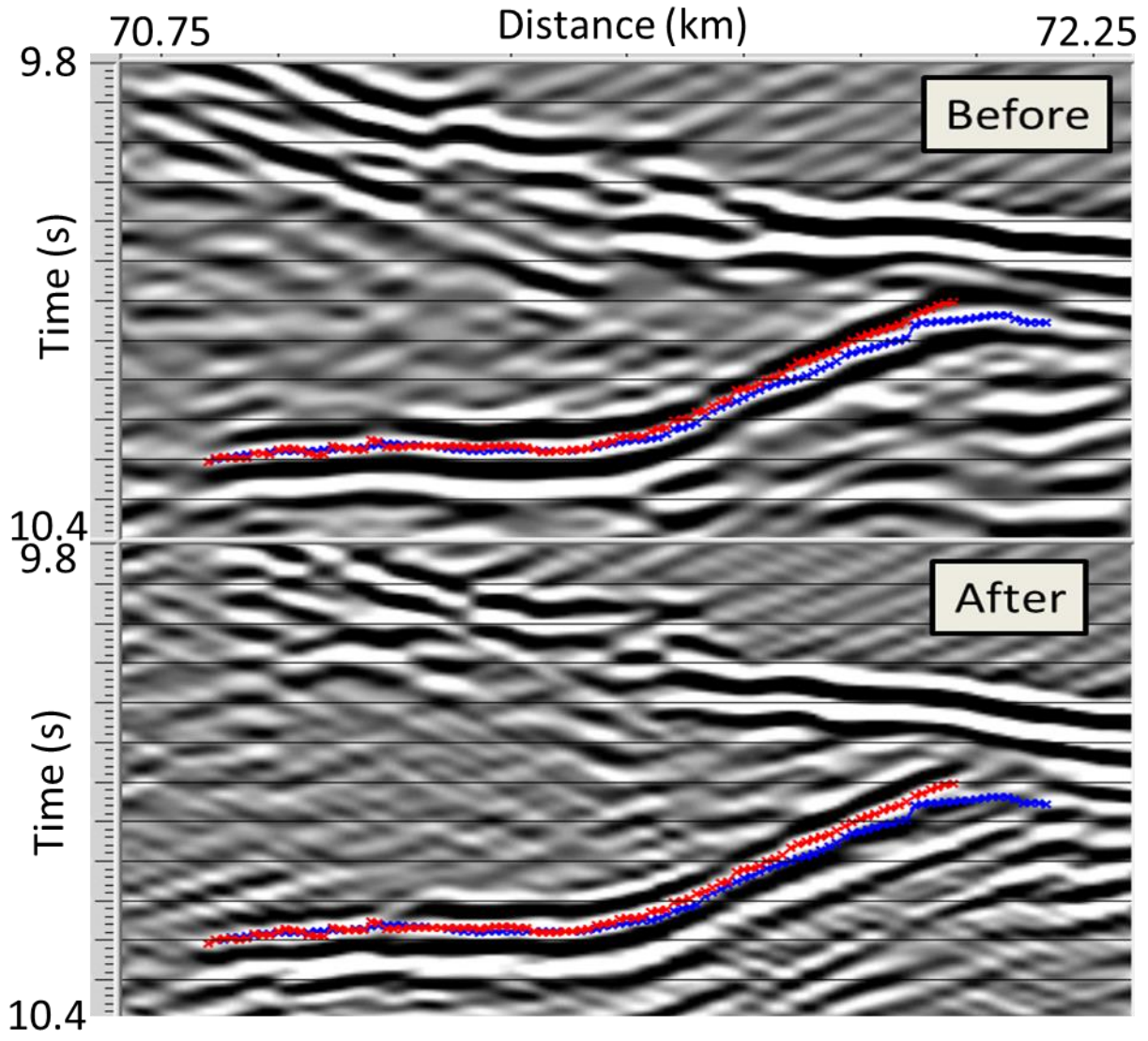
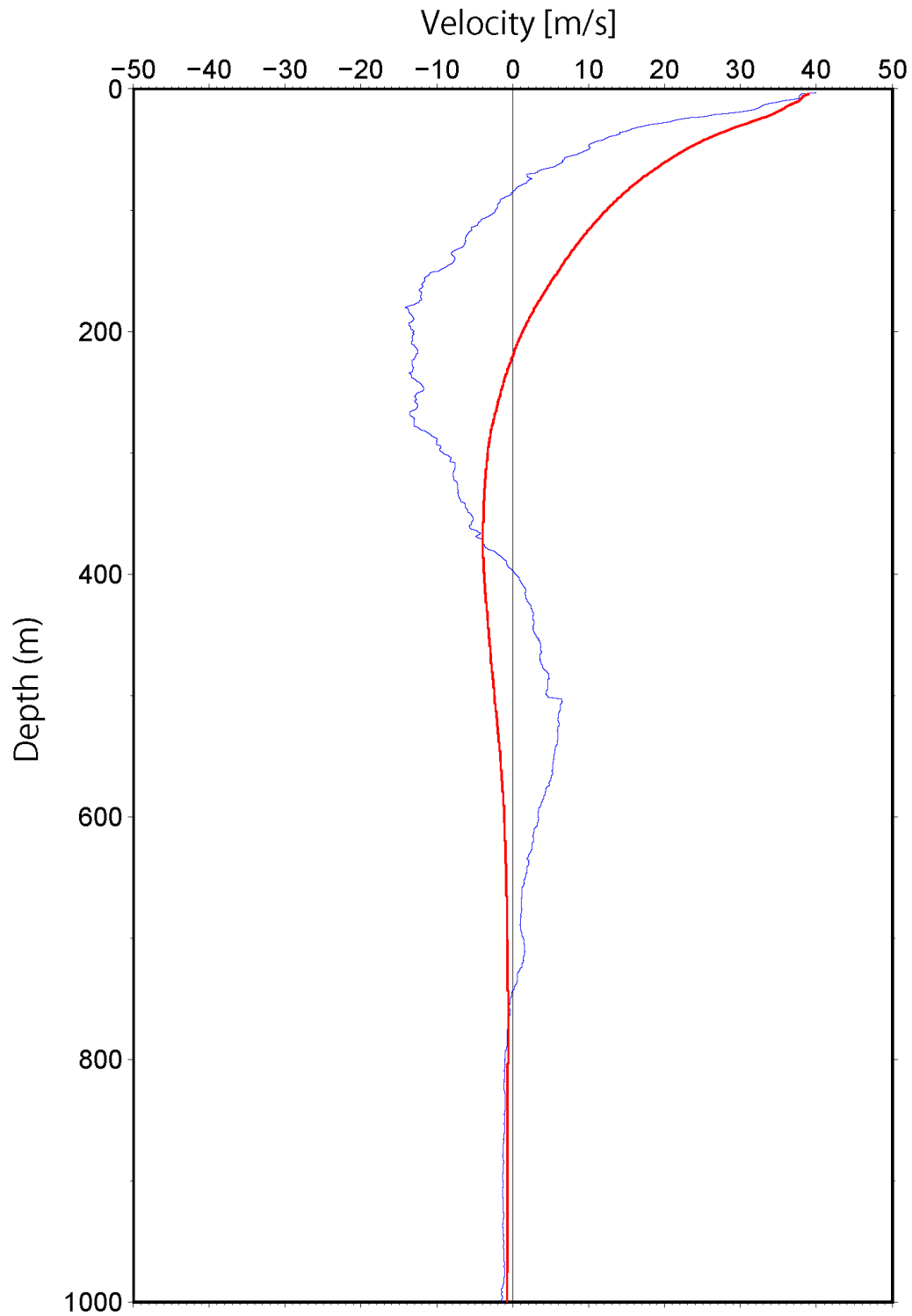


Figure 11. Zoomed time lapse seismic close to the trench axis. Notice compression effects: Flat reflections (1 and 2) disappearing after the earthquake, and dipping reflections (3 and 4) showing increased lengths after the earthquake, aligning with the dominant sediment flow direction. Direction of rock movements are indicated by green arrows.



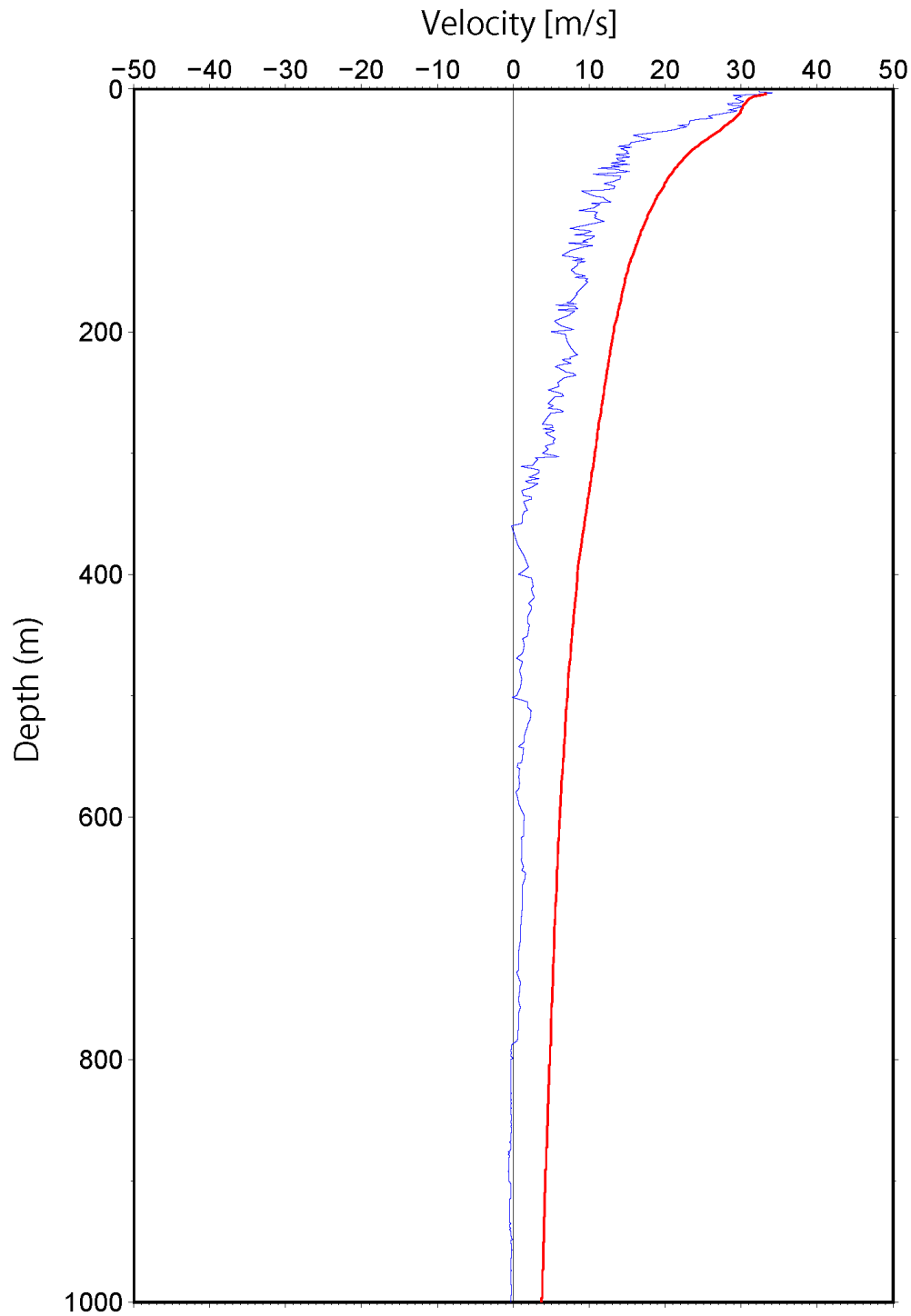
1172
1173
1174
1175
1176

Figure 12. Zoomed detail of the seismic data before (top) and after the earthquake demonstrating horizontal compression: the dip is increasing (red line) after the earthquake.



1177
1178
1179
1180
1181
1182
1183

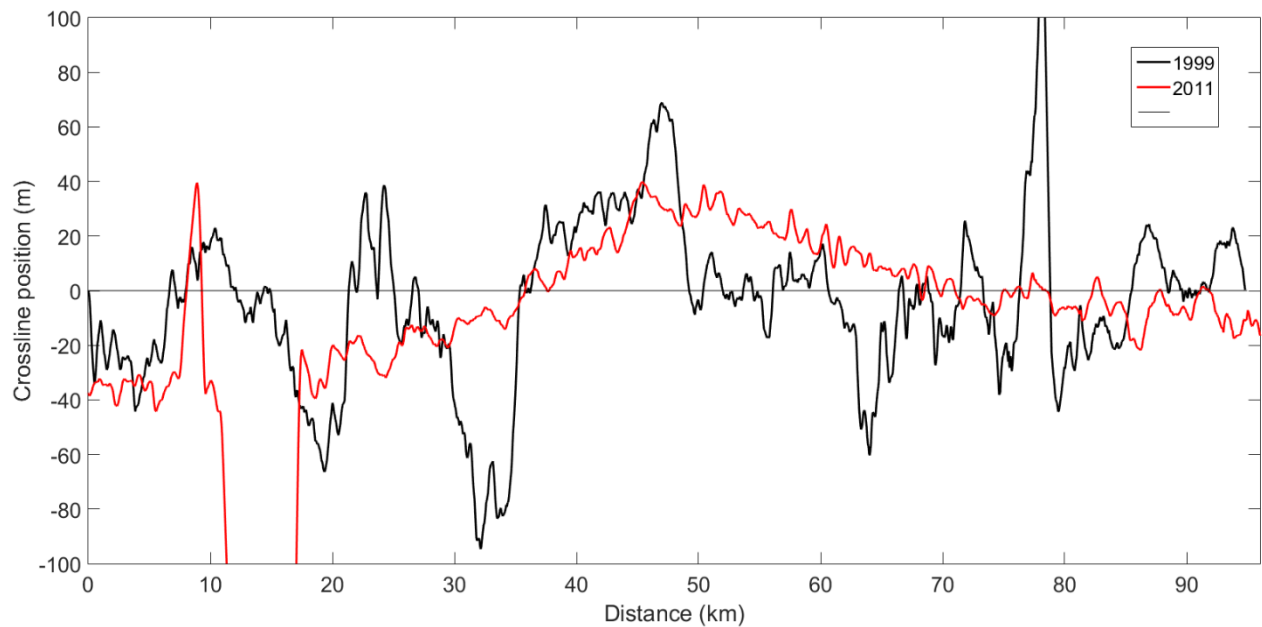
Figure A1. Estimated water velocity difference between May (1st to 31st) 2011 and September (15th August to 15th September) 1999 (blue curve). The red curve shows the corresponding cumulative average velocity change. Notice that the velocity change is less than 1 m/s at 1000 m depth.



1184
1185
1186
1187
1188
1189
1190
1191

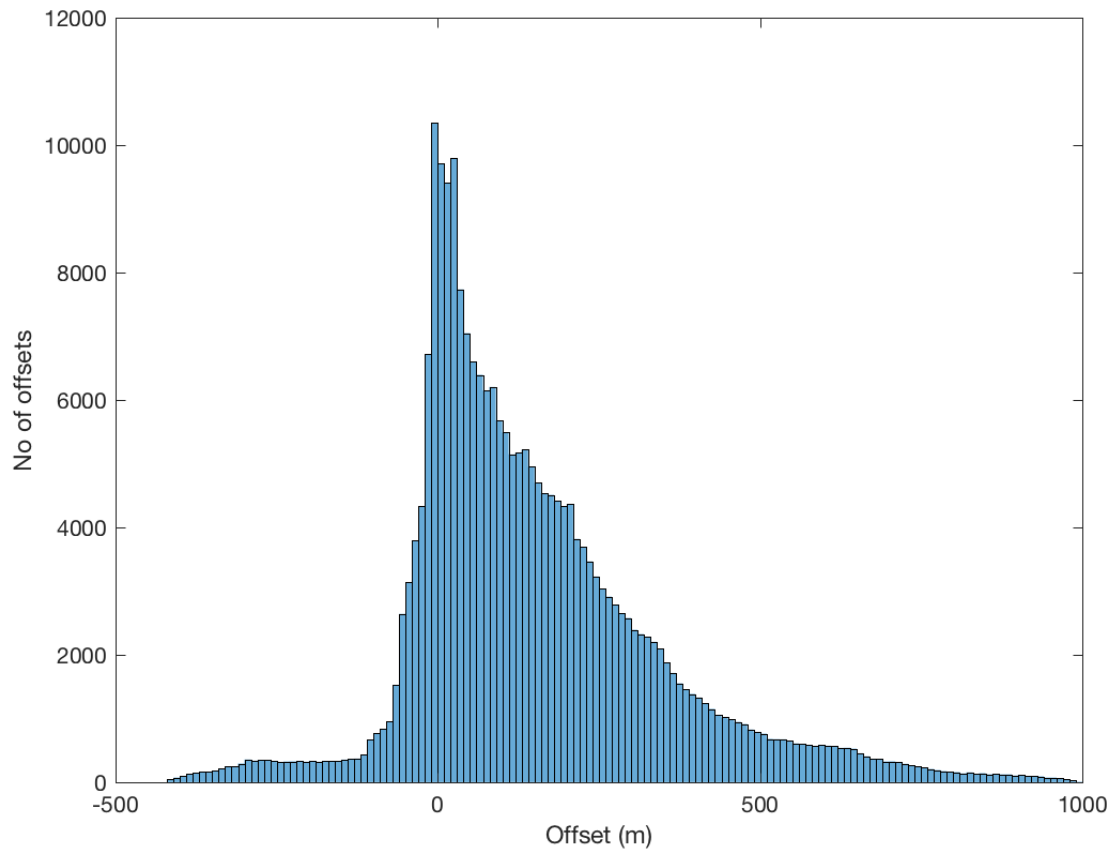
Figure A2. Estimated water velocity difference between May (1st to 31st) averaged over all years from 1999 to 2011 and September (15th August to 15th September) for the same years. The red curve shows the corresponding cumulative average velocity change. Notice that the velocity change is less than 4 m/s at 1000 m depth.

1192
1193
1194
1195
1196
1197
1198
1199



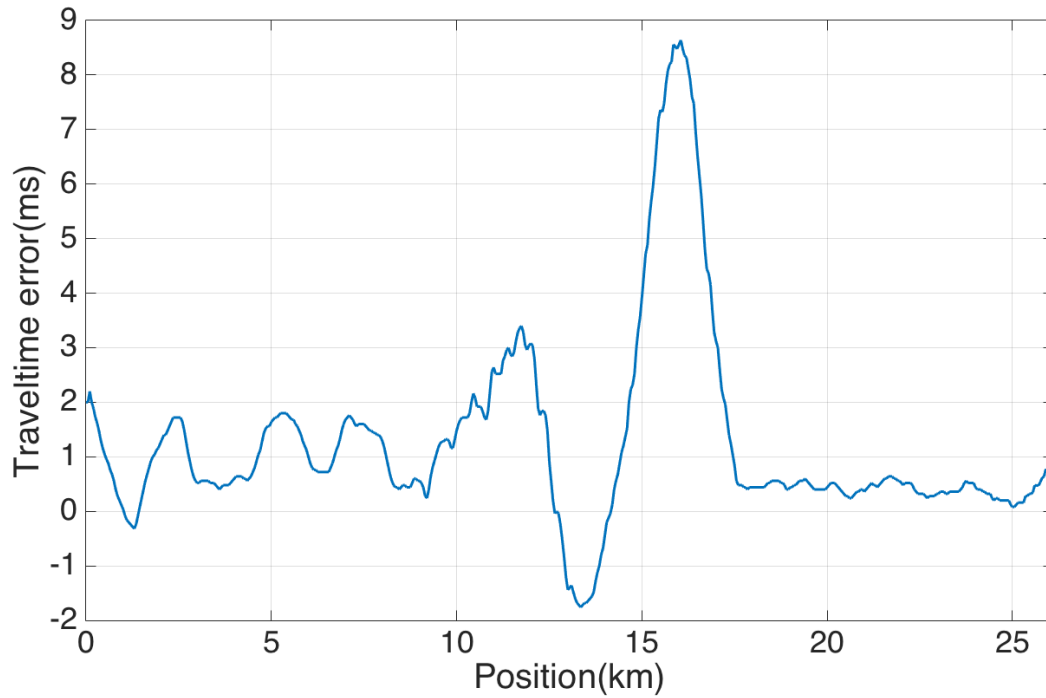
1200
1201
1202
1203
1204

Figure B1. Shot positions relative to a straight line (at zero) for the 1999 (black) and 2011 (red) data. There is a large mis-positioning between 11.5 and 17 km, up to 500 m. Apart from this, the positioning errors are less than 100 m.



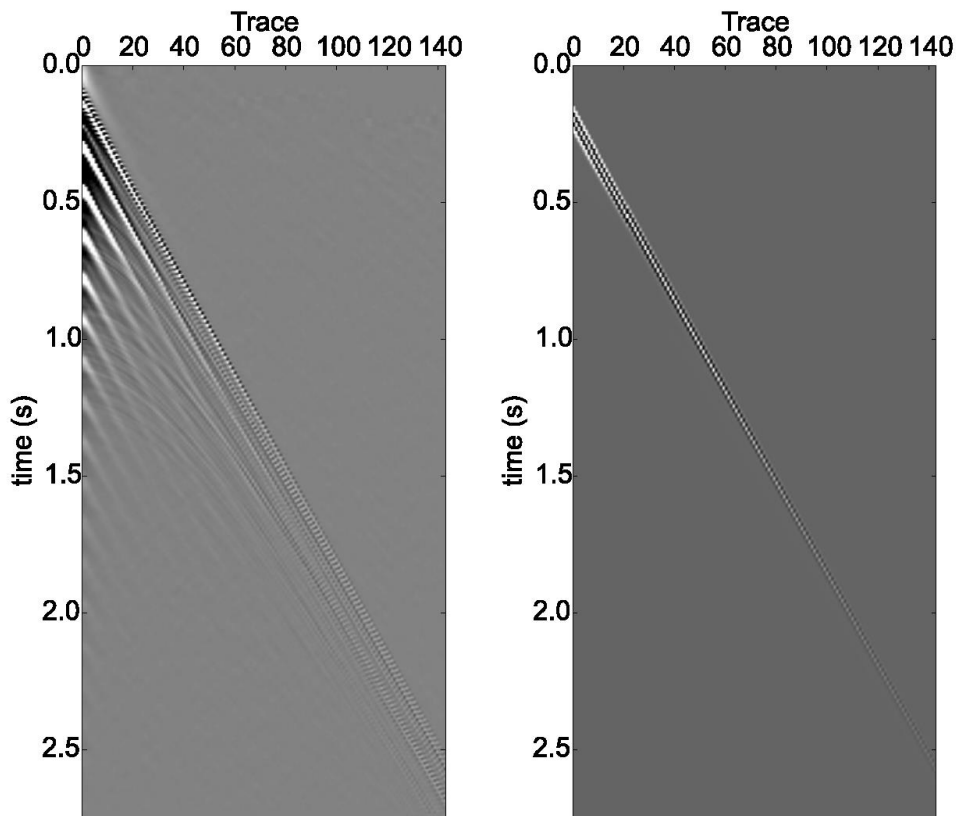
1205
1206
1207
1208
1209
1210

Figure B2. Crossline offset distribution for the MY101 (1999) survey.



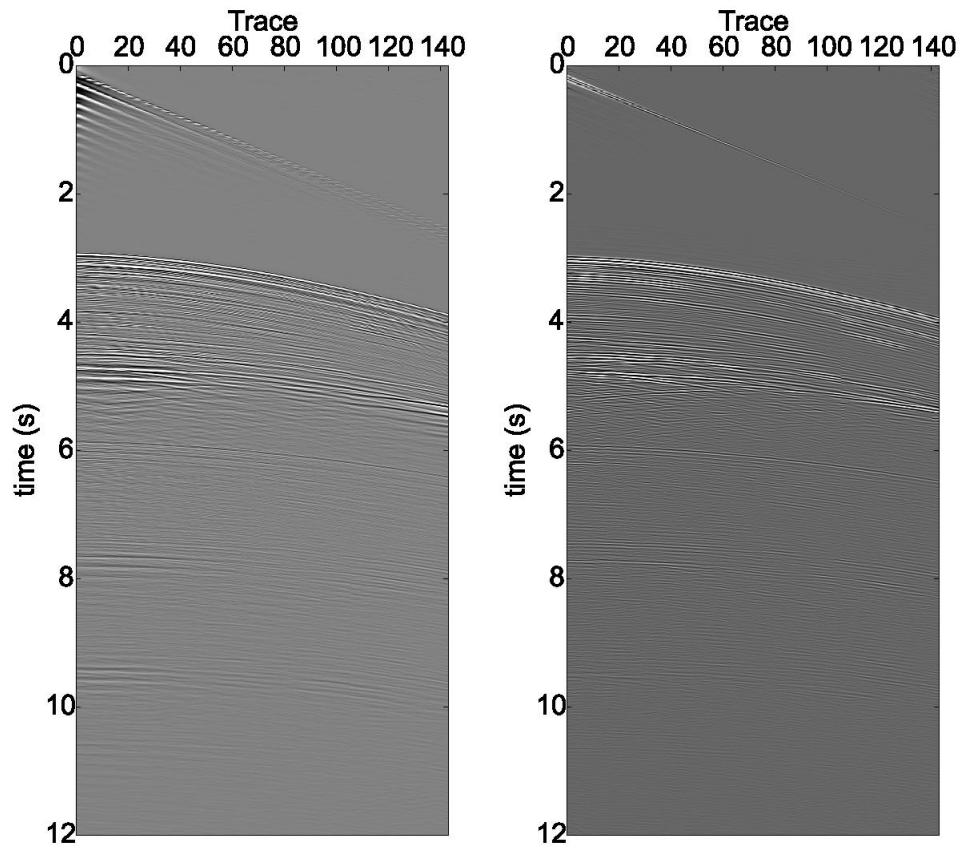
1211
1212
1213
1214
1215
1216
1217
1218

Figure B3 Travel time error of the sea bottom reflector based on a 3D synthetic dataset. The seismic model used to create the data was built using the bathymetry from the area around the survey line.



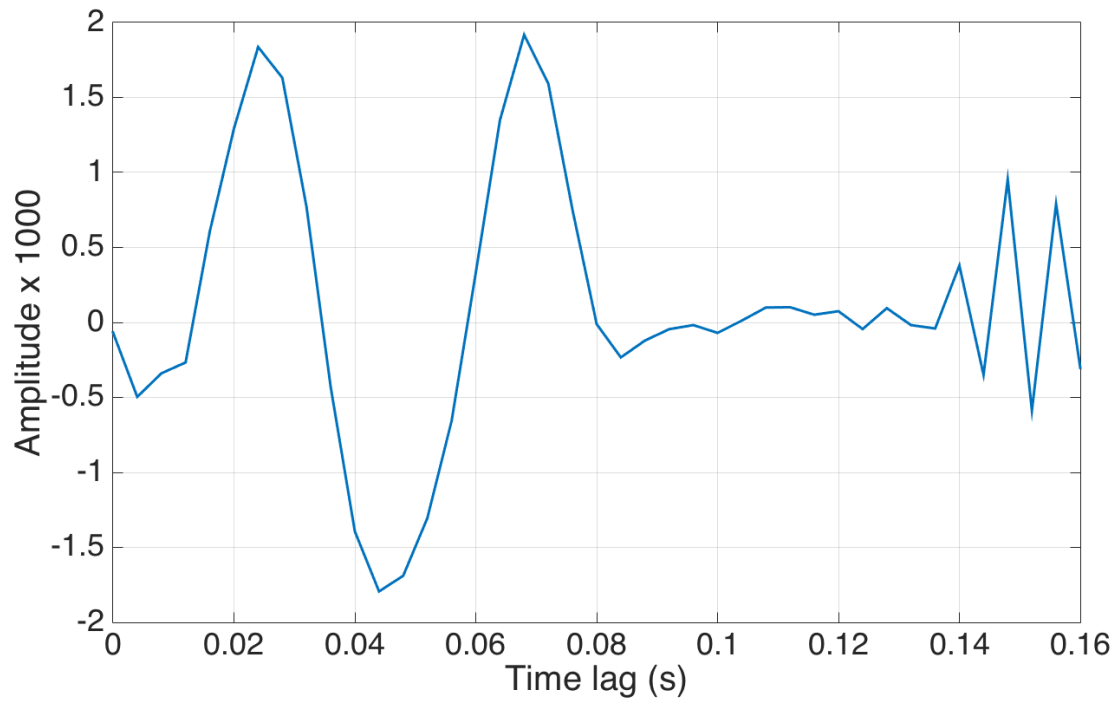
1219
1220
1221
1222
1223
1224
1225
1226

Figure B4 Input data (left) for estimation of debubble filter. The desired output is shown on the right.



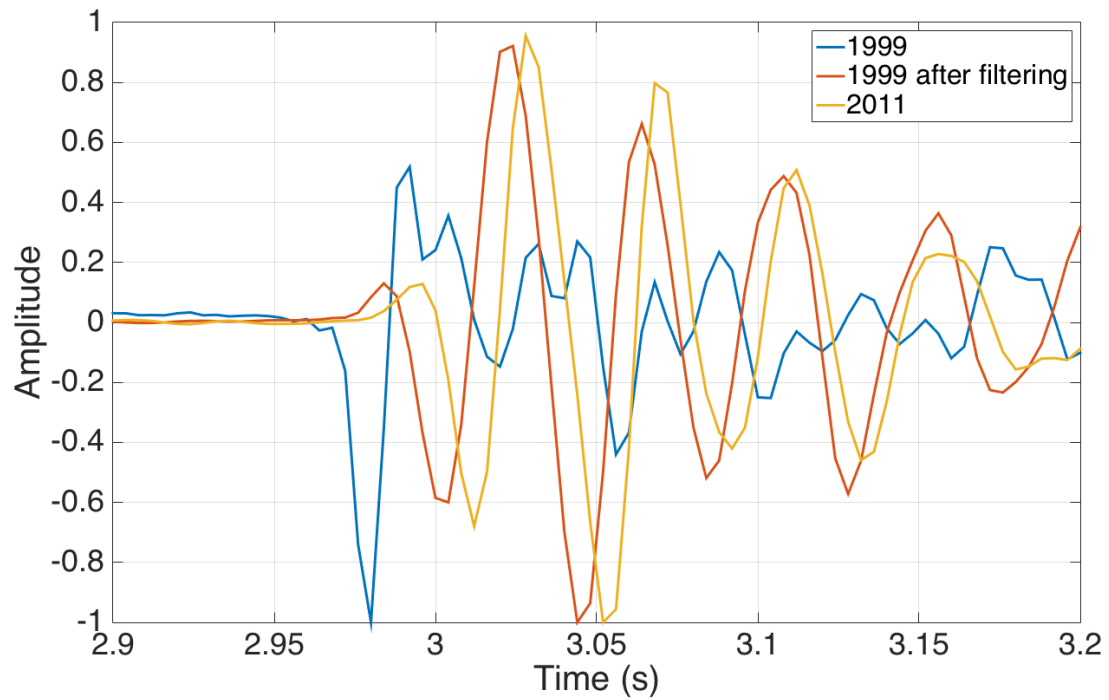
1227
1228
1229
1230

Figure B5 Input shot (left) and the output after debubble (right).



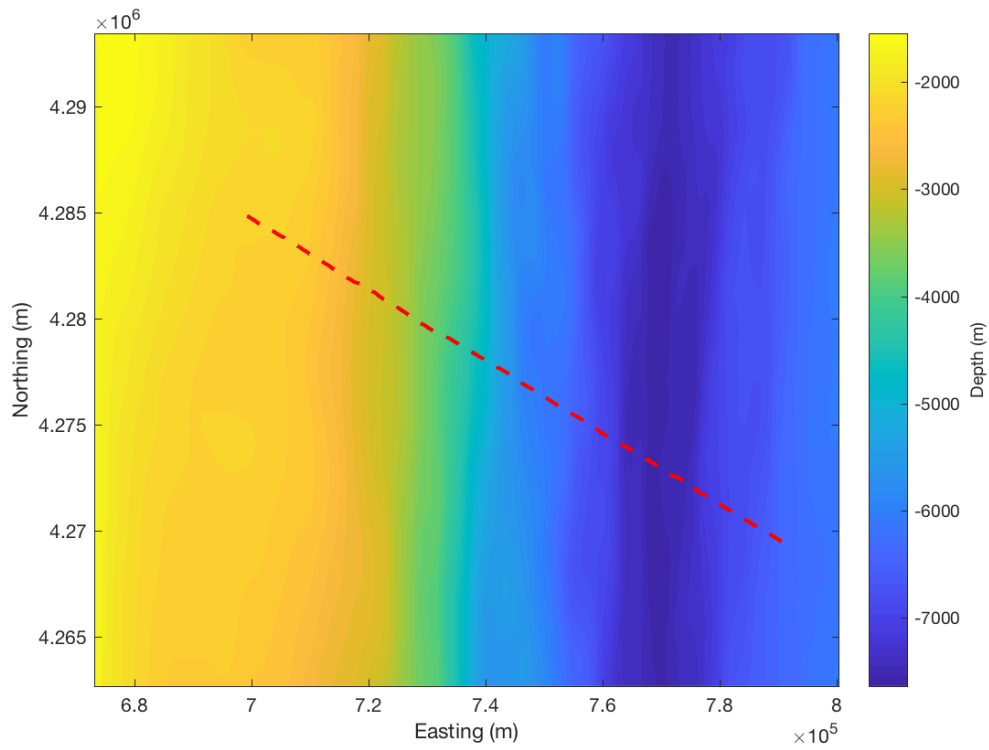
1231
1232
1233
1234
1235
1236
1237
1238

Figure B6 Global match filter used to match the MY101 (1999) survey to the D13 (2011) survey



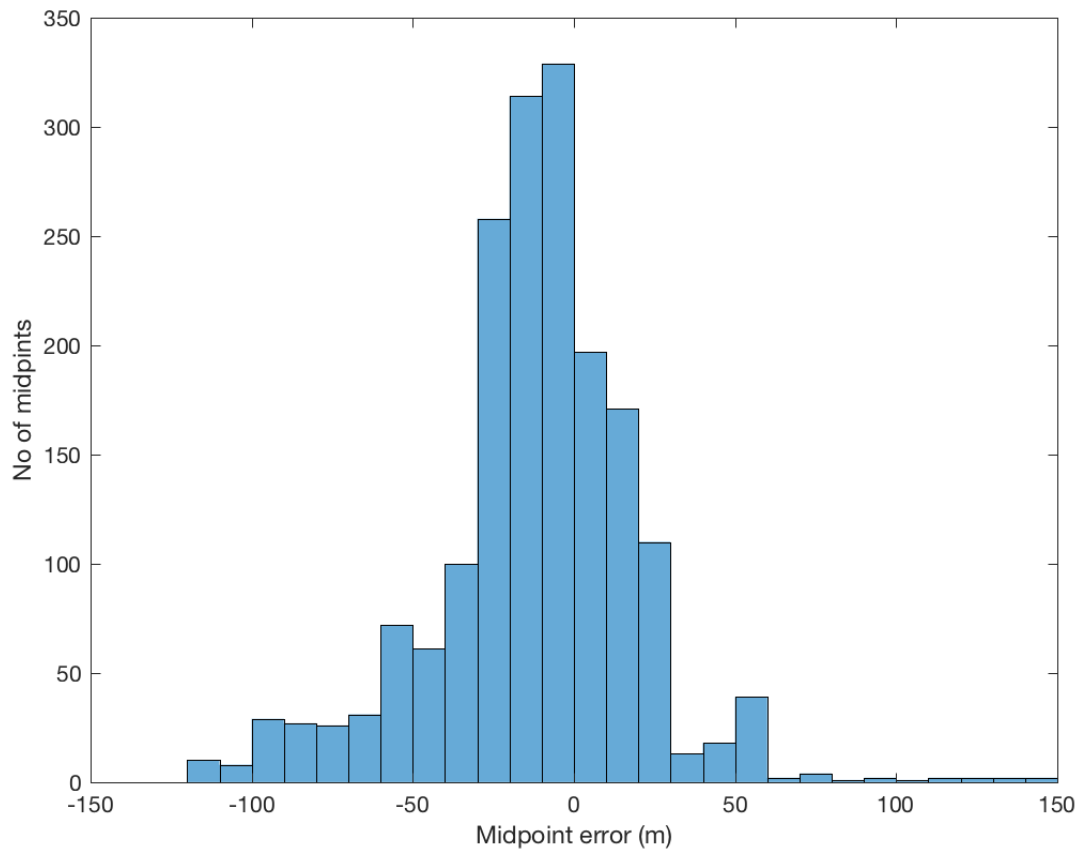
1239
1240
1241
1242
1243
1244
1245

Figure B7 Comparison of the seabed reflection before and after global matching. The traces have an offset of 150 m and picked from shots at a position of 5km from the start of the survey.



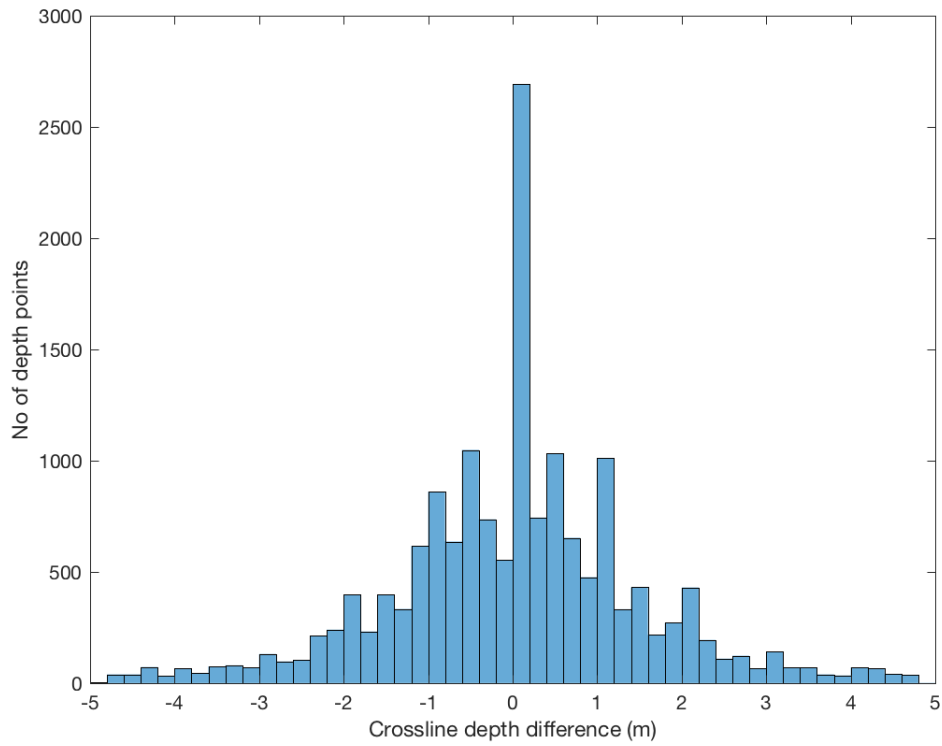
1246
1247
1248
1249

Figure B8. Bathymetry of the area surrounding the 1997 line. The red dashed line indicates the survey line.



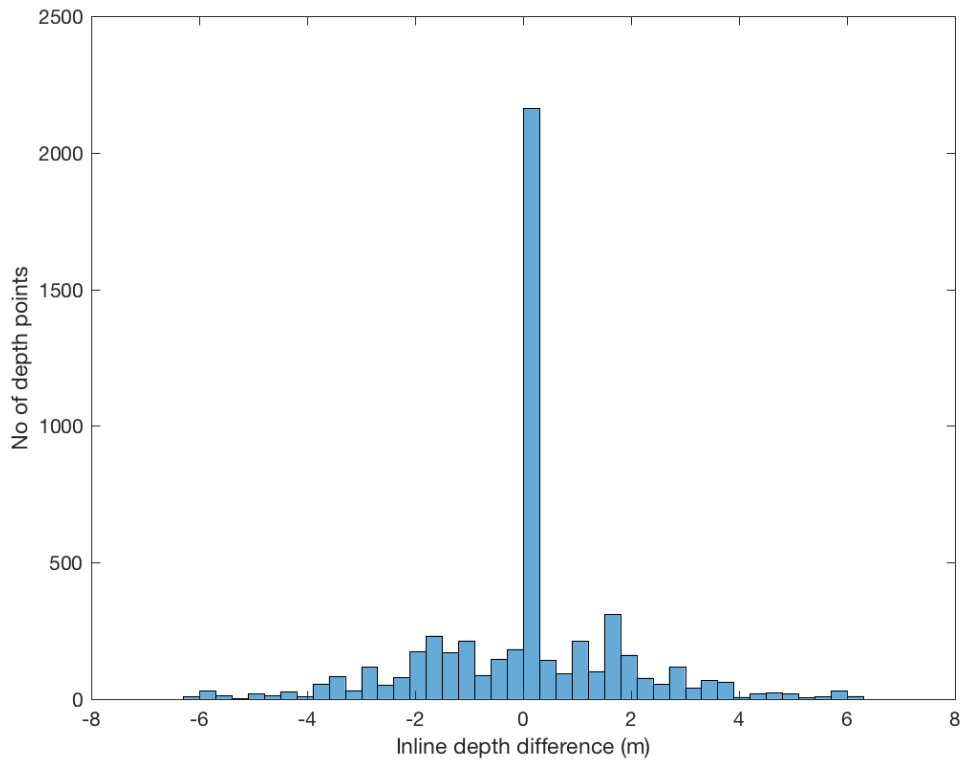
1250
1251
1252
1253

Figure B9. Near offset midpoint position error in the cross-line direction.



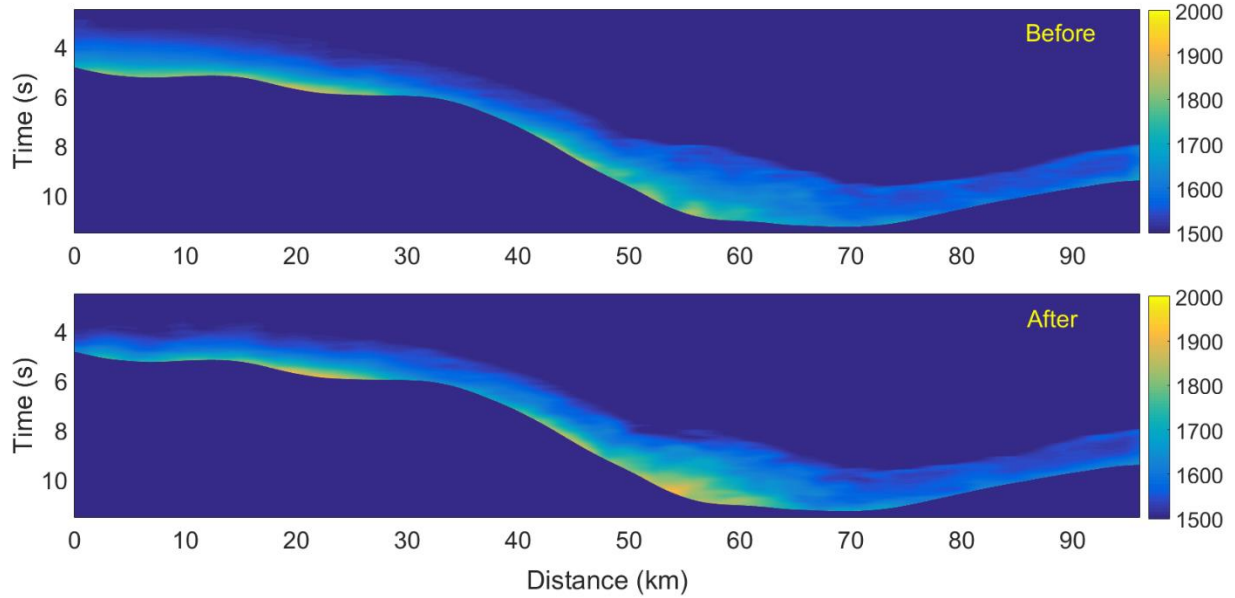
1254
1255
1256
1257
1258
1259
1260

Figure B10. Seafloor depth differences calculated along lines extending 100 meters on each side of survey shot points in the North-South direction. The depth difference is relative to the depth of the seafloor at the survey shot points.



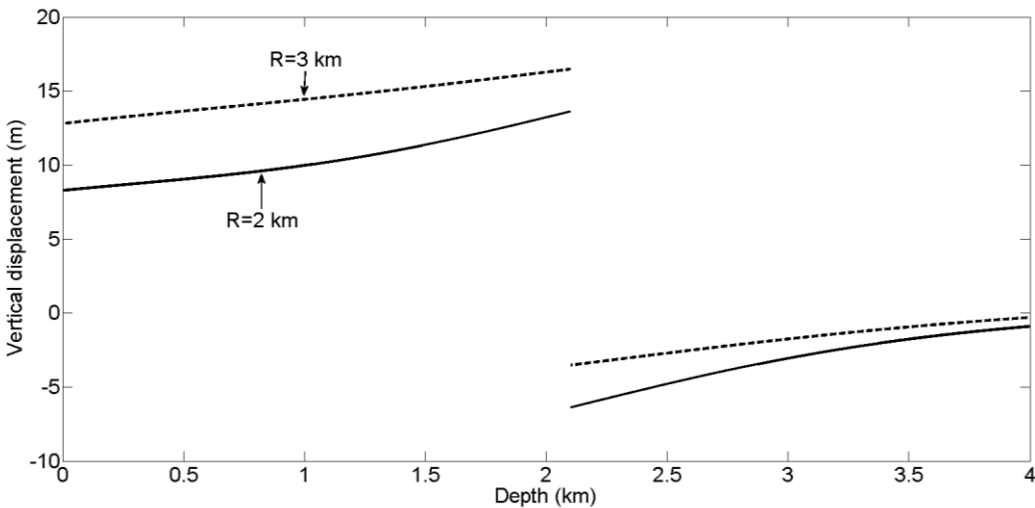
1261
1262
1263
1264
1265
1266
1267
1268
1269

Figure B11. Seafloor depth differences calculated along lines extending 25 meters on each side of survey shot points in the East-West direction. The depth difference is relative to the depth of the seafloor at the survey shot points.



1270
1271
1272
1273
1274
1275
1276

Figure C1. Stacking velocities before (top) and after (bottom) the earthquake. Notice that the velocities for the sub-sediment rocks have been set to 1500 m/s.



1277
1278
1279
1280
1281
1282
1283
1284

Figure D1. Modeled vertical displacement versus depth (measured from seabed) using Geertsmaa's equation for a cylinder radius of 2 and 3 km radius, respectively. Here we assume that the sediment package is 2.1 km thick and we observe that a seabed subsidence of 8.2 m corresponds to approximately 13.8 m subsidence at the sediment-basement interface (2.1 km), corresponding to an overburden stretch of 5.6 m. For a 3 km radius, the corresponding stretch is less, 3.8 m. In the modeling we have used $H_0 = 10$ m and a Poisson ratio of 0.25.